Gravimetric Constraints on the Hydrothermal System of the Campi Flegrei caldera

N. Young[1], R. Isaia[2], J. Gottsmann[1*]

[1]School of Earth Sciences, University of Bristol, United Kingdom
[2] Istituto Nazionale di Geofisica e Vulcanologia (INGV), Osservatorio Vesuviano, Italy

Key Points:

- Hydrothermal plumbing of the central sector of the Campi Flegrei is controlled by volcano-tectonic structures
- Three shallow-seated (< 1.5 km depth) hydrothermal feeder systems are imaged at Pozzuoli, Solfatara/Pisciarelli volcano and Astroni volcano
- Low densities of feeder systems are explained by porous caldera-fill material with between 0.38 and 1 vapour volume fraction and between 0 and 0.62 liquid volume fraction in secondary void space

Corresponding author: J. Gottsmann, `gljhg@bristol.ac.uk`

Abstract

The Campi Flegrei caldera (Italy) has been undergoing unrest over the past five decades including episodes of rapid ground deformation, seismicity and variations in gas emissions. Hydrothermal fluids and gases are released most vigorously in the central sector of the caldera at the fumarolic fields of Solfatara volcano and Pisciarelli. We conducted a high-precision gravity survey coupled with inverse modelling to image the shallow (<2 km depth) structure of the hydrothermal feeder system. Results indicate the presence of three anomalously low density bodies beneath Pozzuoli, Astroni volcano and the Solfatara/Pisciarelli fumarolic fields. The first two are inferred to be sealed hydrothermal systems trapped beneath impermeable cap rock while the latter depicts a plume-like geothermal feeder system reaching the surface via a combination of Solfatara's maar-diatreme structure and the intersection of NW-SE and NE-SW trending regional faults. The density contrasts of the reservoirs from background values are best explained by a multiphase mixture of caldera-fill containing a secondary and interconnected void volume fraction of between 0.2 and 0.3 that hosts a vapour volume fraction ψ_v of between 0.38 and 1 and a liquid volume fraction ψ_l fraction of between 0 and 0.62. This work highlights the control of volcano-tectonic structures on fluid movement in the shallow crust of hydrothermally active volcanic systems undergoing sustained or periodic unrest.

1 Introduction

Volcanic unrest is often characterised by anomalous seismicity, gas emissions and surface deformation, and is usually attributed to sub-surface magma movement (Sparks, 2003). Volcanic calderas have complex sub-surface structures resulting not at least from the vertical collapse of a pre-existing volcanic edifice and often host both extensive hydrothermal and magmatic reservoirs (Gottsmann & Battaglia, 2008). Hydrothermal systems are a complex interface between magma reservoirs and the surface (Todesco, 2008) and not only produce measurable unrest signals but also modulate geophysical and geochemical signals from underlying magma reservoirs (Chiodini et al., 2002; Gottsmann & Battaglia, 2008; Todesco, 2008; Ingebritsen et al., 2010; Chiodini et al., 2016).

Campi Flegrei caldera (CFc) is a well-documented restless caldera where the separation of the signals from magmatic and hydrothermal sources has not been trivial (Troise et al., 2019). Solfatara volcano and neighbouring Pisciarelli (Fig. 1) host the main surface features of the hydrothermal system at CFc and are located $\sim$ 2.5 kilometres to the

NE of Pozzuoli, the centre of ground deformation over the last 50 years (Di Giuseppe et al., 2015) of unrest. Our current understanding of the structure and dynamics of the hydrothermal system at CFc is informed predominantly by geochemical constraints, geophysical data and resulting models (Caliro et al., 2007; Bruno et al., 2007; Troiano et al., 2019): a multiphase plume of vapour and liquid fuelled by the interaction of magmatic and meteoric fluids at depth rises to feed fumaroles and mud-pools at the surface (Chiodini et al., 2015). While significant sub-surface density variations are expected from this model, gravity data have not been used to contribute to the understanding of the shape and size of the shallow-seated (< 1.5 km) hydrothermal feeder system. Here, we present results from a new gravimetric survey of the central sector of the CFc including a high-resolution gravity survey of Solfatara volcano coupled with data inversion to image the density structure of the upper-most part of the hydrothermal system.

2 Background

2.1 Campi Flegrei Caldera Structure and Recent Unrest History

Campi Flegrei caldera is a $\sim$ 13-km-wide volcanic caldera in the Campanian Plain near Naples, Italy (Vitale & Isaia, 2014) formed by two major vertical collapses at $\sim$ 40 ka (Giaccio et al., 2017) and $\sim$ 15 ka (Deino et al., 2004). Post-collapse eruptive activity over the last 15 ka generated at least 70 eruptions, mainly concentrated in the central eastern sector of the caldera (Smith et al., 2011; Bevilacqua et al., 2015). More than 20 eruptions occurred in the epoch of activity from 5.8 to 3.8 ka forming landmarks such as Astroni volcano and Agnano caldera (Isaia et al., 2009; Smith et al., 2011), with the latest magmatic eruption in 1538 AD creating Monte Nuovo volcano (Barberi et al., 1984).

The vertical collapses and long-term ground deformation have divided the caldera floor into a block structure (Orsi et al., 1999). The dominant fault trends within the caldera are NW-SE and NE-SW (Di Vito et al., 1999; Florio et al., 1999; Vitale & Isaia, 2014; Isaia et al., 2015) in addition to caldera ring faults (Berrino et al., 2008; Barberi et al., 1991; Gottsmann et al., 2006; Zollo et al., 2003).

The caldera fill is composed of intercalated lava flows, pyroclastic material, and marine and continental sediments (Rosi & Sbrana, 1987; Piochi et al., 2014). Gravity data depict the fill as a broad ($\sim$6 km wavelength) low density anomaly (Barberi et al., 1991; Capuano et al., 2013). Drilling encountered a zone of thermo-metamorphic rocks below the fill at depths between 2.5 km and 3.1 km, several small igneous intrusions, high thermal gradients of 100-170 $\mathrm{K\,km^{-1}}$ and locally raised isotherms in the central-eastern part (Piochi et al., 2014) of the caldera.

Episodes of rapid uplift and subsidence have been recorded at CFc since Roman times (Parascondola, 1947; Bellucci et al., 2006), though subsidence has been the dominant long-term trend (Barberi et al., 1984). Episodes of rapid ground uplift occurred in 1969-72 and 1982-84 totalling 3.5 m near Pozzuoli (Barberi et al., 1984). Bucking a trend of slow ground subsidence since 1989, numerous mini-uplift events have occurred producing deformation on the order of centimetres accompanied by seismic activity (Chiodini et al., 2010, 2015) followed by a new episode of sustained uplift beginning in 2005. Fumarolic flow rate, discharge temperature and seismicity increased at Solfatara volcano and Pisciarelli from 2006 onwards and an increased magmatic contribution was inferred from the composition of the fumarolic gases (Chiodini et al., 2016; Giudicepietro et al., 2019). The cause of the rapid meter-scale uplifts is still controversial with magmatic and hydrothermal sources or a mix of both identified as contributors (Troise et al., 2019). Many authors suggest that the more recent mini-uplift events have an exclusively hydrothermal origin (Gottsmann et al., 2006; Manconi et al., 2010; D'Auria et al., 2011; Amoruso et al., 2014; Chiodini et al., 2015). NW-SE faults are reactivated during uplift and subsidence and may be important pathways for the upward movement of gas and magma to the surface (Vilardo et al., 2010)

2.2 Solfatara volcano and its fumarolic fields

Solfatara volcano is the most thermally active part of the caldera (Di Giuseppe et al., 2015). It releases ten times more thermal energy than the conductive heat flux across the entire caldera floor (Chiodini et al., 2001). Hydrothermal gases and fluids are released most vigorously at Solfatara volcano's crater floor and its easter inner wall as well as at the Pisciarelli fumarolic field located on its NE flank (Fig. 1) (Caliro et al., 2007). The 100° C isotherm resides only a few hundred metres below the surface of Solfatara's crater (Piochi et al., 2014).

The main hydrothermal features within Solfatara's crater include a mud-pool named La Fangaia and two main fumaroles named Bocca Nuova and Bocca Grande (see Fig. 1). Detailed geological mapping by (Isaia et al., 2015) identifies Solfatara's structure as a maar-diatreme. High angle normal faults characterise the crater edges and fault planes are predominantly NW-SE. Two lava domes reside in the NE and S crater walls. The crater itself is embedded in the older structure of the Agnano-Monte Spina Complex and fumaroles and hydrothermal activity are concentrated in the fault zones and their intersections, where highly fractured rocks act as preferred pathways for fluid ascent.

2.3 The Hydrothermal Plume

The presence of a hydrothermal plume beneath Solfatara volcano was first suggested by Cioni et al. (1984) who, based on geochemical data, proposed that dry steam separates from a geothermal liquid at 236° C in a highly fractured zone to feed the fumarole fields. Further compelling evidence was presented by Chiodini et al. (2015) based on fumarole geochemistry, CO_2 flux, water table heights, seismic velocity and InSAR data as well as by thermo-hydro-mechanical modeling (Todesco & Berrino, 2005; Coco et al., 2016). The numerical models require the multi-phase flow of ascending hot fluids (H_2O and CO_2) from depth through a porous medium to reproduce measured fumarole emissions, ground deformation and gravity changes. The current conceptual model of the plume suggests that rising magmatic gases flash hydrothermal liquids in a deep 'mixing zone' and form a gas plume which ascends to the surface (Caliro et al., 2007; Chiodini et al., 2015). A summary of relevant geophysical and geochemical surveys of Solfatara volcano and the wider CFc is given in Table 1.

3 Methods

3.1 Data Acquisition

We performed a new static gravity survey from 8-12 July, 2015 using a Scintrex CG-5 Autograv gravimeter (serial number: 572) in tandem with a TOPCON HiPer Pro Dual-Frequency GNSS base and rover system. The survey area encompassed the highly urbanised central sector of the CFc (Fig. 2) and contained a total of 85 benchmarks laid out in two different spatial networks.

Benchmarks within Solfatara crater were ordered in a dense irregular grid with a minimum spacing of 17 m and included a local gravity control point. The remainder of the benchmarks were spaced more widely along the roads around Solfatara volcano with an average spacing of 1 km and a maximum spacing of 2.5 km. The different spacing permitted us to investigate the expression of the hydrothermal plume at Solfatara volcano at a similar scale to several local geophysical studies while also exploring the spatial distribution of the hydrothermal system across the central sector of the CFc (Fig. 2). Both the GPS reference receiver and the main gravity base station were located near Monte Nuovo and all gravity measurements were tied to this reference. The entire network covered an approximate area of 36 km^2 and the precision of repeat measurement was $\pm 15\,\mu$Gal (average of 12 cycles of 30s long readings of 6Hz raw data at each benchmark). Urban noise led to an average standard error of individual gravity measurements of ± 8 μGal which is a factor of between 3 and 5 higher than usually attainable during quiet conditions.

We recorded GNSS data for 5-20 min at 1Hz at the survey benchmarks using a roving receiver/antenna unit. The base receiver/antenna unit recorded continuously at 1 Hz during the survey period. The derived precision of the benchmark locations was generally under 0.05 m in the vertical and better than 0.04 m in the horizontal after baseline processing of the benchmark locations against the base station which in turn was processed against three permanent reference stations of the local INGV Osservatorio Vesuviano Permanent Global Navigation Satellite System (GNSS) network and three regional International GNSS Service (IGS) references (NOT1, MAT1, MEDI).

3.2 Gravity Data Reduction and Correction

The objective of a static gravity survey is to obtain information about the sub-surface density distribution. The magnitude of gravity at any point is influenced by latitude, elevation, topography of the surrounding terrain, Earth and Ocean tides, sub-surface density variations and instrumental drift (Telford et al., 1991). Raw gravity data are therefore composed of several contributions and require careful corrections to obtain the component reflecting sub-surface density variations only, known also as the Bouguer anomaly (BA). Earth tides and instrumental drift are removed first to obtain the observed gravity (g_{obs}) from which the BA can be obtained.

$$BA = g_{obs} - g_n + FAC - BS + TC, \tag{1}$$

where g_n is the normal gravity, FAC is the free-air correction, BS is the Bouguer slab correction and TC is the terrain correction. A detailed description of the data reduction is given in the Supplementary Information.

3.3 Data Detrending

The regional Bouguer anomaly is controlled by both shallow and deep-seated density distributions. Long-wavelength features (e.g., spatial variations in deep-seated bedrock thickness) must be removed to reveal the local Bouguer anomaly caused by shallow-seated structures. We calculate a regional gradient of 0.86 mGal/km with a strike of N50°E from the regional Bouguer anomaly data and derive the linearly-detrended residual anomaly (LRA) data for further investigation. Our regional trend compares to a regional gradient of 0.5 mGal/km and a strike of N35°E presented by Cassano and La Torre (1987) who use a much larger and wider-spaced dataset. The Topex gravity data (Sandwell et al., 2013) with a spatial coverage and average station spacing matching more closely with our survey gives a regional gradient of 0.2 mGal/km with a strike of N37° E.

To test the robustness of our results we detrended our data using the regional trend from the Topex data set. While the amplitudes of the resultant anomalies of course change, the presence and location of the main anomalies remain. Therefore, even using the lowest quoted regional gradient, we obtain model results that are reproducible and robust.

Removing a linear trend may not be appropriate in structurally complex areas such as collapse calderas to investigate anomalies associated with a shallow-seated hydrothermal system. Large scale gravity surveys at CFc have consistently shown a negative gravity anomaly associated with low density caldera fill (Nunziata & Rapolla, 1981; Berrino et al., 2008; Capuano et al., 2013). We explore the effect of the fill on our data by constructing a forward model based on the most recent gravity data presented by Capuano et al. (2013) and borehole density data (Barberi et al., 1991; Piochi et al., 2014). The caldera fill is simulated by stacked spheroids within a cylindrical volume of 2 km thickness and 3 km in radius with a density contrast of -300 $\mathrm{kg\,m^{-3}}$, centered offshore of Pozzuoli (see Supplementary Information Figure S5). Capuano et al. (2013) suggest that the uppermost part of the caldera fill contains remnant high density feeder systems, as well as post-collapse lava flows and domes. We therefore set the top of the model at a depth of 1 km and subtract the simulated caldera-fill anomaly from the regional Bouguer anomaly data. We thus obtain a second local anomaly: the caldera-fill detrended residual anomaly (CRA).

Values for the LRA and CRA anomalies are reported relative to the base station at Monte Nuovo. Secondary anomalies of Solfatara volcano have their values calculated from average background values of Solfatara's crater floor. Relative values are provided so that the anomalies are comparable across the two detrended datasets.

3.4 Total Horizontal Gravity Gradiometry

First and second horizontal derivatives of Bouguer gravity data are useful to study structural controls on gravity anomalies (Cooper & Cowan, 2008). The first derivative highlights boundaries of buried bodies or faults. The second derivative yields inflection points of the first gradient and reveals absolute maxima/minima which provide information on the shape of buried bodies or inclination of density interfaces. The total horizontal gradients are obtain from

$$\mathrm{THD1} = \sqrt{\left(\frac{\partial g}{\partial x}\right)^2 + \left(\frac{\partial g}{\partial y}\right)^2}, \tag{2}$$

where THD1 is the first total horizontal derivative, $\partial g/\partial x$ is the change in gravity in the x direction and $\partial g/\partial y$ is the change in gravity in the y direction (Cooper & Cowan, 2008). Similarly

$$\mathrm{THD2} = \sqrt{\left(\frac{\partial^2 g}{\partial x^2}\right)^2 + \left(\frac{\partial^2 g}{\partial y^2}\right)^2}, \tag{3}$$

where THD2 is the second total horizontal derivative (Fedi, 2002).

3.5 Inverting the Local Bouguer Anomaly Data

We invert the resultant Bouguer gravity data (LRA and CRA) to image causative density contrasts at depth using GROWTH2.0 (Camacho et al., 2002, 2011). GROWTH2.0 divides the model space into 3D parallelepiped elements and obtains a 3D anomalous density model using prescribed (a priori) density contrasts. Inherent non-uniqueness in the inversion is addressed by using a mixed minimisation condition which selects a solution based on least-squared model fitness and model smoothness, or the total anomalous mass. Model inputs include the Bouguer gravity data, cell size, the density contrast with background density and a balance factor. The balance factor determines the complexity of the model of positive and negative density contrasts with high balance factors producing simple models. Densities with too high a contrast produce isolated skeletal bodies and densities with too low a contrast produce inflated and interconnected bodies. Both constraints must be explored to find an appropriately complex model with a plausible density contrast and low auto-correlation (Camacho et al., 2011). As a result, the minimisation of residuals is insufficient to establish the suitability of the model for given density contrasts. A mixed minimisation procedure which balances the goodness-of-fit criterium (model fitness) with the total anomalous mass (model smoothness) minimisation condition is applied to select the optimal model. We explored the model space for each dataset iteratively, searching for suitably complex anomalous bodies and low auto-correlations for a low cell resolution and repeatedly increasing the resolution and retesting of the density contrast and balance factor at each iteration. A $50\,\mathrm{kg\,m^{-3}\,km^{-1}}$ increase in background density was implemented to prevent oversizing of anomalous bodies with increasing depth during the inversion.

We tested density contrasts in the range of ±300 to ± $600\,\mathrm{kg\,m^{-3}}$ and balance factors from 10 to 40 (producing in total 119 model solutions) and selected the model with the lowest auto-correlation for given model smoothness. This methodology effectively uses a classic trade-off between model misfit and model simplicity (Gubbins, 2004). The best solution balances a compromise between adequately fitting the data and producing a suitably simple model. While the model with the best goodness-of-fit has an auto-correlation of 0.06 and a balance factor of 20 it yields an array of skeletal bodies of anomalous densities and does not satisfy the mixed minimisation criteria for an optimal solution. Our optimal model of the CRA has an autocorrelation of 0.13 and a balance factor of 40 after 58 iterations, while the optimal model of the LRA has an autocorrelation of 0.14 and a balance factor of 40 after 61 iterations. Details on the inversion procedure and sensitivity tests are given elsewhere (Camacho et al., 2002, 2011).

4 Results

4.1 The Bouguer Anomaly

The amplitudes of all anomalies are orders of magnitude above the uncertainties associated with individual measurements or the terrain correction and are therefore robust indicators of sub-surface density variations. Figs. 3a-c show the distribution and amplitudes of the regional and local Bouguer anomalies (LRA and CRA). Linear detrending (Fig. 3b) reveals a broad (∼ 4 km wide) and negative (∼ -6 mGal)) anomaly centered northwest of Solfatara volcano. It is composed of three distinct lows near Pozzuoli, Solfatara volcano and Astroni volcano. The Pozzuoli anomaly is not present in the CRA data (Fig. 3c) and the overall negative anomaly is significantly reduced in both wavelength and amplitude ($\sim$ 0.4 km and $\sim$-4 mGal, respectively) and its centre shifted towards the north. The gravity lows between Solfatara volcano and Astroni volcano persist. Anomalies at the periphery of the survey are poorly constrained and hence ignored.

When looking in more detail at the Solfatara area, the patterns of the LRA and CRA anomalies are similar, but with noticeable differences in the negative amplitudes (from average values of the crater floor) of the respective gravity lows . The main gravity low in the eastern part of the crater is -1.1 mGal in the LRA from an average value of -3.15 mGal and -0.76 mGal in the CRA from an average value of 1.42 mGal (Fig. 4a and b). In both cases, the lows are located close to the fumaroles of Bocca Nuova and Bocca Grande and extend eastwards towards Pisciarelli. There are gravity highs on the north-northeastern and southern edges of the crater in both datasets, but the north-northeastern high is strongest in the LRA data.

While there is a small gravity low ($\sim$-0.3 mGal amplitude from background levels in the crater floor) in the vicinity of La Fangaia in the LRA data (Fig. 4a), this anomaly is only very weak in the CRA data (Fig. 4b).

4.2 Horizontal Derivatives

The first horizontal derivative of the LRA (Fig. 5a) reveals strong gradients along the northeastern crater wall of Solfatara, around the edge of the low gravity region between La Fangaia and Bocca Grande and more subdued gradients around La Fangaia and elsewhere in the crater. Prevailing NNE-SSW and NW-SE trends are highlighted by the gradients (Fig. 5b). The second horizontal derivative suggests similar fault trends (Fig. 5c and d). The structural trends obtained from total horizontal gravity gradiometry closely match field observations (Fig. 5e and f).

4.3 Sub-surface Distribution of Anomalous Mass

The optimal LRA and CRA models have a balance factor of 40, an auto-correlation of 0.14, and an a priori density contrasts of -450 to +450 $\mathrm{kg\,m^{-3}}$ (Fig. 6). The models image three main bodies of negative density contrast beneath Pozzuoli, Astroni volcano and Solfatara volcano. Although it is difficult to directly relate mathematically derived density contrasts with rock density contrast, the optimal density range matches the 1σ range in rock densities about an average of 2300 kg/m^3 encountered in boreholes from Campi Flegrei (Piochi et al., 2014). Despite their inherent non-uniqueness, the models consistently provide robust results on the density variations at depth for different a priori density contrasts (Supplementary Figures S6 and S7). The dominant anomalous negative density bodies persist in all inversions, although as expected they become larger and more interconnected with decreasing a priori density contrasts.

The optimal LRA inversion images the Solfatara/Pisciarelli anomaly as approximately 0.5 km wide and extending from close to the surface to 0.8 km below sea level. The anomalous body beneath the Pozzuoli area is 1 km in diameter at its widest and extends from ~0.5 km to 1.2 km depth. It is slightly elongated in the NNE-SSW direction. The Astroni anomaly is elongated E-W, 1.75 km across its widest point and extends from 0.5 km to 1.4 km depth (Fig. 6).

The optimal anomalous bodies imaged by the CRA inversion are similar to those found for the LRA. However, the Pozzuoli anomaly vanishes and the anomalous bodies are imaged at a slightly shallower depth (Fig. 6). The long axis of the Astroni anomalous body is shifted slightly towards the north with respect to the LRA body.

Fig. 7 shows the surface traces of the -600, -450 and -300 $\mathrm{kg\,m^{-3}}$ density isosurfaces. The inversions of both the LRA (Fig. 7a) and the CRA data (Fig. 7b) consistently image the Astroni and the Solfatara/Pisciarelli anomalies in the same locations. The Solfatara/Pisciarelli anomaly covers the SE edge of Solfatara crater and extends to Pisciarelli in both cases. The Astroni anomaly is centered SW of Astroni crater and covers its SW wall. The imaging and co-location of the Astroni and Solfatara/Pisciarelli anomalies in both models is an indication of the robustness of the inversion, while the veracity of the Pozzuoli anomaly remains uncertain.

5 Discussion

5.1 Imaging of distinct reservoirs: Sub-surface controls on fluid distribution

We present the first gravimetric image of the hydrothermal system at Campi Flegrei caldera. Inversions of two differently-detrended data sets (LRA and CRA) provide robust and reproducible results and image two low-density reservoirs beneath Astroni and Solfatara volcanoes, which we interpret as shallow-seated, fluid-rich hydrothermal reservoirs. An anomaly beneath Pozzuoli is only imaged by one of the models, which may be attributed to the lack of offshore gravity data in this survey, potentially preventing us to properly account for the effect of the caldera fill on the data at Pozzuoli. Both model results for Pozzuoli are plausible and alternative evidence is required to support the existence or absence of a low-density reservoir beneath Pozzuoli (see below).

The optimal modeled negative density anomalies indicate a ∼20% reduction in subsurface density from background values. This can be explained by a porous and fractured caldera-fill containing hydrothermal fluids. Borehole data indicate drained host rock (dominantly volcanic tuff) densities ρ_r between 1600 and 2200 kg m^{-3} in the top 1 km beneath the caldera containing between 5 and 40 vol% inherent void space (Piochi et al., 2014). To explain the modeled negative density contrasts a reduction in background bulk host rock density is required. In the hydrothermally active areas imaged in this study this can, for example, be achieved by the generation of additional (secondary) void space by fracturing and/or hydrothermal dissolution (scenario 1) or replacing the liquid phase in undrained porous host rock by a vapour phase (scenario 2). In the former case, the background bulk densities will be those reported above while, in the latter case undrained bulk densities of the caldera-fill are in range of 1650 to 2500 kg m^{-3} for given porosities.

We first explore scenario 1 of bulk density reduction from an average background host rock density ρ_r of 1900 kg m^{-3}. Assuming that the reduction in density is primarily driven by the creation of new void space ϕ that is fully connected and can host hydrothermal fluids in either vapour (density ρ_v=1.5 kg m^{-3}) and/or liquid (density ρ_l=1000 kg m^{-3}) form, the optimal anomalous density contrast $\Delta\rho$ of the reservoirs of ∼ -400 ±25 kg m^{-3} can be explained by a multi-phase mixture of caldera-fill containing an additional interconnected void volume fraction of between 0.2 and 0.3 that contains a vapour volume fraction ψ_v of between 0.38 and 1 and a liquid volume fraction ψ_l fraction 0 and 0.62 . The parameter space of conceivable fractions of solids and voids (filled with vapour and/or liquid) that fit the optimal model for this scenario is shown in Fig. 8 and can be reproduced by

$$\Delta\rho = (1-\phi)\rho_r + \phi\psi_l\rho_l + \phi\psi_v\rho_v - \rho_r. \quad (4)$$

Given the borehole rock porosity and density ranges, the second end-member scenario (vapour replaces liquid in undrained caldera-fill) is only feasible in rocks containing inherent connected void fractions of 0.4 or more in order to explain the optimal density contrast, and is hence if at all only relevant for the top few hundred meters beneath the surface (Piochi et al., 2014). While the most plausible interpretation of the optimal models is a combination of processes associated with both explored scenarios, to explain the modeled density contrast at depths $>$ 250 m scenario 1 must be dominant and from our gravity contrast model alone we favour the creation of additional void space. However, additional constraints are available to help explore the scenarios further.

The permeability structure of the central part of the caldera is key to understanding the distribution of fluids at the time of the survey. Hot low-density fluids will rise from their source until they attain neutral buoyancy, reach the surface or encounter a barrier to flow, i.e., a zone of reduced permeability. The results suggest the presence of fluid-rich bodies trapped beneath the surface of the CFc at Pozzuoli and Astroni volcano while one body discharges freely at Solfatara volcano and Pisciarelli. This implies the presence of an impermeable seal preventing access of fluids to the surface at Pozzuoli and Astroni volcano. Geochemical and electric data indicate the presence of a two-phase hydrothermal plumbing system at the CFc with a gas-dominated regime residing at shallow (few tens to hundreds of meters) depth beneath the centre of the caldera (Chiodini et al., 2011; Gresse et al., 2017).

Permeabilities measured in-situ in boreholes at the CFc vary over 4 orders of magnitude ($<10^{-18}$ to $>10^{-14}$) (Piochi et al., 2014). Total Horizontal Gradiometry of Solfatara volcano (Fig. 5) shows a correlation of the geometry of low density bodies with the main fault and fracture systems mapped in the field (Isaia et al., 2015). The combination of in-situ rock permeability and fracture/fault permeability may explain the distribution of surface expressions of hydrothermal activity in the caldera and their spatio-temporal evolution. Alunitic alteration at the Solfatara and Pisciarelli hydrothermal fields increases rock porosity and permeability and reduces density (Mayer et al., 2016). Critically stressed faults can be hydraulically conductive (Jasim et al., 2015), while mineralisation can seal previously connected pathways within or around a fault (Sibson, 1994). Faults can thus be both permeable pathways and impermeable inhibitors for fluid flow, depending on the stress regime and degree of alteration. Fluids themselves can modulate permeability via thermally induced hydraulic fracturing (Knapp & Knight, 1977;

Cusano et al., 2008; Saccorotti et al., 2007). Permeability in hydrothermal systems is not static and changes constantly due to fracturing and cementation from hydrothermal precipitation, meteroic water invasion or tectonic stresses (Rowland & Sibson, 2004). Faults at the CFc present fluid pathways on timescales of 1-10 years and 10^2-10^3 years (Vilardo et al., 2010). It is hence conceivable that geophysical surveys conducted over the past few decades at the CFc provide different snapshots of a constantly evolving hydrothermal system. We therefore compare and contrast the Pozzuoli, Astroni and Solfatara/Pisciarelli anomalies imaged by our study with published results from other investigations (see also Table 1).

5.2 The Pozzuoli anomaly

Several studies found evidence for a shallow-seated hydrothermal reservoir beneath Pozzuoli, but its nature is contested:

- Vanorio et al. (2005) use seismic velocity tomography to delineate a zone of high V_p/V_s ratios (2.3) beneath Pozzuoli centred at approximately 0.8 km depth and 0.8 km in radius. Below this, they image a low V_p/V_s (1.4) anomaly at 4 km depth. They interpret these features as a brine caused by steam condensation and a gas enriched formation, respectively.
- Chiarabba and Moretti (2006) find a high V_p/V_s region below Pozzuoli at 0-2 km depth, overlying a low V_p/V_s anomaly at 3 km depth which they interpret as steam condensation and gas accumulation, respectively.
- Seismic attenuation tomography by De Siena et al. (2010) in tandem with V_p/V_s ratios image an anomaly 0-2 km below Pozzuoli, with a $\sim$1 km radius. The nature of this anomaly (liquid or gas dominated), however, remains ambiguous in the study.
- Chiodini et al. (2015) and Caliro et al. (2007) use geochemical models to predict the vaporisation of fluids at 2 km depth which then rise to the surface.
- A stacked (gas-rich pockets beneath liquid dominated systems) arrangement of fluids is predicted by fault-controlled fluid flow modelling for CFc (Jasim et al., 2015).

In summary, the available evidence is inconclusive regarding the nature of a shallow-seated reservoir beneath Pozzuoli with indications for either vapour or liquid dominated regimes. One aspect that needs consideration is the potential for temporal change in the sub-surface phase relationships. Chiarabba and Moretti (2006) and M. Battaglia et al. (2006) use combined data from 1984 and from 2001, while Vanorio et al. (2005) and De Siena et al. (2010) used data from 1984, only. Not only do the combined datasets risk masking of temporal signals, but the system may change over the course of 15 years. Temporal changes in elasticity of the upper crust have been suggested for CFc (Di Luccio et al., 2015). Cycles of sealing, fracturing and resealing are implied on timescales of decades to centuries, for example, at Yellowstone caldera where drill cores plugged almost completely after 25 years (Dobson et al., 2003; Ingebritsen & Sorey, 1988). Our modelling results are consistent with either a liquid or vapour dominated system with the caveat that a liquid-dominated regime requires a significantly higher connected porosity compared to a vapour-dominated system to explain the gravity data (Fig. 8).

5.3 The Astroni anomaly

The Astroni anomaly is unexpected as there are no records of fumaroles or other geothermal manifestations in the area. The anomaly is located at the convergence of two crater walls and one might expect high density material here compared to adjacent low density crater fill. However, there are several geophysical anomalies associated with Agnano caldera (Isaia et al., 2009), in which Astroni volcano is nested:

- Astroni volcano is seismically active (Chiodini et al., 2017; Saccorotti et al., 2007). de Lorenzo et al. (2001) and De Siena et al. (2010) image a seismic anomaly beneath Agnano at 0-3 km depth which they relate to a high temperature aquifer.
- Capuano et al. (2013) identify an E-W elongated low-gravity anomaly at Astroni volcano at 1-2 km depth, which they interpret as a low density gas-rich reservoir with secondary mineral precipitation as a mechanism for preventing surface expression. They suggest that hot gases condense near the surface and generate a water table which in the Agnano plain forms lake Agnano.
- Troiano et al. (2019) identify a highly resistive (vapour-rich) anomaly corresponding to the south-eastern edge of the Astroni crater, while the Agnano plain is characterised by a mainly conductive anomaly.
- Water from the Agnano well has high P_{CO_2} values, less negative carbon isotope signatures than meteoric water and high ${HCO_3}^{-2}$ concentrations, indicating a con-

tribution of heat and hydrothermal fluids from a magmatic system (Venturi et al., 2017).

In light of these geochemical and geophysical observations we suggest that the gravity anomaly of Astroni volcano is formed by a liquid-dominated highly fractured geothermal reservoir trapped beneath a less permeable cap rock. Localised seismicity may be due to the movement of fluids along faults and it is plausible that there are pathways linking Solfatara/Pisciarelli and Astroni volcano via a network of mainly NW-SE and NE-SW to NNE-SSW trending faults.

5.4 The Solfatara/Pisciarelli anomaly

The key features of the Bouguer anomalies at Solfatara/Pisciarelli are i) the gravity highs on the SW and NE crater walls of Solfatara(>0.5 mGal), ii) the gravity low on the southeastern side of Solfatara's crater floor (>-1 mGal) and adjacent Pisciarelli and iii) the moderate gravity low near La Fangaia (∼-0.3 mGal) (Fig. 4). These compare to the findings from an earlier survey of Solfatara (Oliveri del Castillo et al., 1968): i) an elongate ∼ 1 mGal gravity high on the NE crater wall, ii) two connected gravity lows reaching from the southern edge of La Fangaia (∼ -0.3 mGal) to Bocca Grande and Bocca Nuova (∼ -0.4 mGal), and iii) a small scale ∼ -0.3 mGal gravity low in the western side of the crater (see Fig. 9). Bruno et al. (2007) demonstrated the spatial correlation of the first three anomalies of the 1968 survey with areas of maximum seismic noise, areas of high CO_2 degassing and elevated temperatures. The horizontal derivative of the 1968 gravity data, highlights the role of faults in concentrating these density anomalies (Bruno et al., 2007).

We divide the anomalies of our survey into three classes (relative to the average gravity of the crater floor), i) low, ii) moderate low and iii) high to discuss their relationship with other recent geophysical observations at Solfatara/Pisciarelli (see Fig. 9 and Table 1).

5.4.1 Low Gravity Class

The low gravity anomaly extends from the eastern side of the crater floor and crosses the crater wall towards Pisciarelli. It coincides with some of the main fumaroles of the geothermal field, which at Solfatara are clustered on its eastern side, where the rocks are intensely fractured (Isaia et al., 2015). We explain the correlation of the gravity low and areas of intense gas emissions in two ways.

Firstly, upwelling vapour replaces water in fractures and pore spaces in the rock causing a local decrease in density.

Secondly, low density material is expected from intense hydrothermal alteration near the fumaroles where connected porosities can reach values of up to 61 vol% (Mayer et al., 2016) with little variation in hydraulic parameters expected to depths of ∼500 m (Montanaro et al., 2016). Proximal areas around the fumaroles should therefore experience a substantial reduction in density due to the coupled effects of fluid flux and alteration.

At the time of the survey the most vigorous fumarolic activity was located at Bocca Nuova, Bocca Grande and Pisciarelli, with no fumarolic activity noted on top of the crater wall. These fumaroles are also the hottest of those in the Solfatara/Piscarelli area (Chiodini et al., 2001). Isaia et al. (2015) have suggested a link between Bocca Nuova, Bocca Grande and Pisciarelli via faulting and fracturing through the crater wall. This region, therefore, may be the main pathway for fluids to ascend from depth. Other fumaroles may be fed less voluminously and/or by narrower, subordinate fracture networks, which are below the spatial resolution capability of the gravity survey. The strongest first and second horizontal gravity gradients (see Fig. 5a and b) are across the crater floor and along the NE crater indicating that the anomalies are strongly influenced by faults and fractures.

Di Giuseppe et al. (2015) found a high resistivity zone close to Bocca Nuova and Bocca Grande, but little correspondence between resistivity and the other fumaroles. The authors attribute the offset between the resistive body and the 1968 gravity low (see Fig. 9) to fluid migration over the time between surveys, but our low gravity anomaly encompasses both the high resistivity body and the 1968 gravity low. Similar to the 1968 survey, our gravity low increases east-wards from the main fumaroles (Fig. 9) towards Pisciarelli.

Solfatara undergoes spatio-temporal variations in ground deformation (D'Auria et al., 2012) and has high levels of seismic noise in an arcuate band from the south to the northeast of the crater floor (Bruno et al., 2007). Saccorotti et al. (2007) show maximum likelihood locations of long-period (LP) earthquakes clustered at 500 m depth beneath the SE rim near Bocca Grande. They interpret the LP signals as due to vibrations of fractures in a buried cavity filled by a water-steam mixture. An interpretation of ultra-high resolution seismic imaging of the centre of Solfatara divides the first 30 m into a shallow zone of aerated tephra underlain by a liquid saturated layer that is deepening in the direction of La Fangaia and a deeper gas accumulation sloping upwards towards the eastern side of the crater (De Landro et al., 2017). Seismic attenuation, a shear-wave velocity anomaly and low V_p/V_s ratios (Chiarabba & Moretti, 2006; De Siena et al., 2010; Chiodini et al., 2015) indicate a shallow gas reservoir around sea level beneath Solfatara.

Byrdina et al. (2014) show high resistivity anomalies in both the crater walls and beneath the crater floor. Bocca Grande is directly above a narrow zone of moderate resistivity and surrounded by a zone of high temperature, high CO_2 and low self-potential. To the east of Bocca Grande is a high resistivity anomaly, and to the west is a low resistivity zone extending towards La Fangaia. Magnetotelluric (MT) and electrical resistivity (ER) data (Troiano et al., 2014, 2019) depict a moderately resistive anomaly below the eastern crater wall and a high resistivity anomaly beneath the main fumaroles and Pisciarelli to 2.25 km depth with a radius of ~ 0.15 km. High-resolution ER tomography images a gas-dominated reservoir at 60 m depth beneath Solfatara's crater floor that feeds Bocca Grande (Gresse et al., 2017).

In summary, we propose that the main gravity low is caused by a shallow-seated (<1000 m depth b.s.l.) accumulation of a two-phase fluid within highly fractured and porous host rocks (Fig. 8). It is plausible that the eastern crater wall is composed of highly altered rocks with elevated porosity compared to the rest of the rim, indicating relict and/or current fluid pathways. The imaged feeder system appears to encompass the most dominant pathway for ascending fluids in the central sector of the caldera through a combination of Solfatara's maar-diatreme structure (Troiano et al., 2019) and its intersection with the dominant fault systems (NW-SE and NE-SW to NNE-SSW) of the caldera.

5.4.2 Moderate Low Gravity Class

A moderate gravity low is located near La Fangaia (Fig. 9) and matches the extent of the 1968 gravity low. The exact location of the shallow-most La Fangaia feeder system is hard to establish as it appears to change with time. Dried up pits were present during the survey which must previously have been mudpools. We therefore use the fencedoff area to delineate La Fangaia (brown shape in Fig. 9), although its most active portion was the southern part of the area at the time of the survey. Gentle first and second horizontal gravity gradients bound La Fangaia and show the same general direction as faults mapped in the field (Isaia et al., 2015) (Fig. 5a and b). The moderate gravity low of La Fangaia is also characterised by high CO_2 flux, low resistivity (with a long lobe extending westwards beneath the surface), low self-potential, high temperature, elevated seismic noise and earthquake clustering (Byrdina et al., 2014) (Table 1). These authors report a positive correlation between CO_2 flux and ground temperature, which are both anti-correlated with self-potential. The lobate geometry of low resistivity is matched by the moderate gravity anomaly beyond the boundary of La Fangaia. Seismic noise is high near the gravity anomaly and has been correlated with anomalous CO_2 degassing (Bruno et al., 2007).

Byrdina et al. (2014) interpret the La Fangaia geophysical anomalies by a liquid saturated plume with both a downwelling condensing liquid water and an upwelling vapour and CO_2 mixture. The water table is locally raised at Solfatara, outcropping at La Fangaia (97 m a.s.l) and only 7 m below the surface at the OAK well nearby (see Bruno et al. (2017)). A two phase (gas and liquid) flow regime feeding La Fangaia is also proposed by numerical modelling (Rinaldi et al., 2011). This suggests that background densities for the crater floor are influenced by the presence of liquid water.

The moderate gravity low is thus likely formed by a CO_2-bearing hot aquifer contained within altered and high-porosity crater-fill.

5.4.3 High Gravity Class

While the depicted gravity highs are constrained only by a low number of benchmarks, the anomalies coincide with the location of the Solfatara cryptodome (northeastern high) and the Mount Olibano lava dome (southern high) (Isaia et al., 2015) (see Fig. 9). The northeastern high matches a gravity high detected by the 1968 gravity survey. Although poor accessibility prevented us from obtaining more measurements on the southern and northeastern rims of the crater, the transition from low density crater fill to the high density Solfatara cryptodome is well marked by a strong first horizontal gradient of the Bouguer anomaly. We therefore interpret the gravity highs as remnant domes forming part of the crater rim.

6 Conclusions

The combined use of high-precision gravity and GPS measurements, high-quality DEMs and 3D data inversion has shed light on the shallow-seated hydrothermal system at Campi Flegrei. The results complement a wealth of existing geophysical and geochemical data for the CFc and lend support to a model of a complex sub-surface hydrothermal structure feeding the active fumarolic areas of the central sector of the caldera. We were able to delineate the shallow-seated two-phase hydrothermal plumbing system beneath Solfatara and Pisciarelli and identified a hydrothermal reservoir beneath the Astroni crater. The main gravity anomalies of Solfatara volcano detected in the new survey broadly match those identified by a previous gravity survey conducted in 1968. However, we show that some smaller anomalies may have evolved in size and location over time. This may indicate that within the resolution capabilities of the Bouguer gravity surveys, Solfatara's main hydrothermal feeder system remained broadly unchanged over the past 50 years with the exception of an enlargement towards Pisciarelli, which over the past 15 years has seen a strong increase of hydrothermal activity. Whether or not a separate hydrothermal system resides beneath Pozzuoli cannot be unambiguously answered by our findings, but there are indications for a shallow-seated low-density hydrothermal reservoir during the time of our survey. We encourage additional geophysical and geochemical studies particularly at Astroni volcano and Pozzuoli to test our model results.

7 Acknowledgments

We are indebted to the INGV for provision of cGPS data and assistance during field work. The work received financial support from two projects funded by the European Commission, Framework Program 7 (grant n° 282759, "VUELCO", and grant n° 308665, "MEDSUV") and the Natural Environment Research Council (grant n° NE/J020052/1). Raw gravity and post-processed elevation data used in this study is available from the National Geoscience Data Centre (NGDC) at http://data.bgs.ac.uk/id/dataHolding/13607565. Topographic data used for gravity data reduction are available on *https://topex.ucsd.edu/cgi-bin/get_data.cgi*, *http://sit.cittametropolitana.na.it/lidar.html* and *http://tinitaly.pi.ingv.it/download.html*. We thank E. van Dalfsen, C. Miller and M. Poland for their thorough and constructive criticisms which helped improve the manuscript.

8 Autor contributions

JG conceived the project and received funding. RI facilitated fieldwork and contributed to data collection. NY and JG collected and processed all gravity and GPS data. N.Y. analysed, modeled and interpreted all data as part of her doctorate. JG took the lead in writing the manuscript based on material presented in NY's doctoral thesis with additional data analysis and interpretation. All authors provided critical feedback and helped shape the final version of the manuscript.

References

Amoruso, A., Crescentini, L., Sabbetta, I., De Martino, P., Obrizzo, F., & Tammaro, U. (2014). Clues to the cause of the 2011–2013 campi flegrei caldera unrest, italy, from continuous gps data. *Geophysical Research Letters*, *41*(9), 3081–3088.

Barberi, F., Cassano, E., La Torre, P., & Sbrana, A. (1991). Structural evolution of campi flegrei caldera in light of volcanological and geophysical data. *Journal of Volcanology and Geothermal Research*, *48*(1-2), 33–49.

Barberi, F., Corrado, G., Innocenti, F., & Luongo, G. (1984). Phlegraean fields 1982–1984: Brief chronicle of a volcano emergency in a densely populated area. *Bulletin of Volcanology*, *47*(2), 175-185. doi: 10.1007/bf01961547

Battaglia, J., Zollo, A., Virieux, J., & Iacono, D. D. (2008). Merging active and passive data sets in traveltime tomography: the case study of campi flegrei caldera (southern italy). *Geophysical Prospecting*, *56*(4), 555–573.

Battaglia, M., Troise, C., Obrizzo, F., Pingue, F., & De Natale, G. (2006). Evidence for fluid migration as the source of deformation at campi flegrei caldera (italy). *Geophysical Research Letters*, *33*(L01307), doi:10.1029/2005GL024904.

Bellucci, F., Woo, J., Kilburn, C. R. J., & Rolandi, G. (2006). *Ground deformation at campi flegrei, italy: Implications for hazard assessment* (Vol. 269). Geological Society.

Berrino, G., Corrado, G., Luongo, G., & Toro, B. (1984). Ground deformation and gravity changes accompanying the 1982 pozzuoli uplift. *Bulletin of Volcanology*, *47*(2), 188-200.

Berrino, G., Corrado, G., & Riccardi, U. (2008). Sea gravity data in the gulf of naples. a contribution to delineating the structural pattern of the phlegraean volcanic district. *Journal of Volcanology and Geothermal Research*, *175*(3), 241–252.

Bevilacqua, A., Isaia, R., Neri, A., Vitale, S., Aspinall, W. P., Bisson, M., ... Rosi, M. (2015). Quantifying volcanic hazard at campi flegrei caldera (italy) with uncertainty assessment: 1. vent opening maps [Journal Article]. *Journal of Geophysical Research: Solid Earth*, *120*(4), 2309-2329. Retrieved from `https://doi.org/10.1002/2014JB011775` doi: 10.1002/2014JB011775

Bruno, P. P. G., Maraio, S., & Festa, G. (2017). The shallow structure of solfatara volcano, italy, revealed by dense, wide-aperture seismic profiling. *Scientific Reports*, *7*(1), 17386.

Bruno, P. P. G., Ricciardi, G. P., Petrillo, Z., Di Fiore, V., Troiano, A., & Chiodini, G. (2007). Geophysical and hydrogeological experiments from a shallow hydrothermal system at solfatara volcano, campi flegrei, italy: Response to caldera unrest. *Journal of Geophysical Research: Solid Earth*, *112*(B6). doi: 10.1029/2006JB004383

Byrdina, S., Vandemeulebrouck, J., Cardellini, C., Legaz, A., Camerlynck, C., Chiodini, G., ... others (2014). Relations between electrical resistivity, carbon dioxide flux, and self-potential in the shallow hydrothermal system of solfatara (phlegrean fields, italy). *Journal of Volcanology and Geothermal Research*, *283*, 172–182.

Caliro, S., Chiodini, G., Moretti, R., Avino, R., Granieri, D., Russo, M., & Fiebig, J. (2007). The origin of the fumaroles of la solfatara (campi flegrei, south italy). *Geochimica et Cosmochimica Acta*, *71*, 3040-3055.

Camacho, A., Fernandez, J., & Gottsmann, J. (2011). The 3-d gravity inversion package growth2.0 and its application to tenerife island, spain. *Computers & Geosciences*, *37*(4), 621-633.

Camacho, A., Montesinos, F., & Vieira, R. (2002). A 3-d gravity inversion tool based on exploration of model possibilities. *Computer and Geosciences*, *28*, 191-204.

Capuano, P., Russo, G., Civetta, L., Orsi, G., D'Antonio, M., & Moretti, R. (2013). The active portion of the campi flegrei caldera structure imaged by 3-d inversion of gravity data. *Geochemistry, Geophysics, Geosystems*, *14*(10), 4681–4697.

Cassano, E., & La Torre, P. (1987). Geophysics. In M. Rosi & A. Sbrana (Eds.), *Phlegrean fields* (Vol. 114, p. 103-131). Quaderni de la Ricerca Scientifica.

Chiarabba, C., & Moretti, M. (2006). An insight into the unrest phenomena at the campi flegrei caldera from vp and vp/vs tomography. *Terra Nova*, *18*(6), 373–379.

Chiodini, G., Avino, R., Caliro, S., & Minopoli, C. (2011). Temperature and pressure gas geoindicators at the solfatara fumaroles (campi flegrei) [Journal Article]. *Annals of Geophysics*, *54*, 151-160.

Chiodini, G., Brombach, T., Caliro, S., Cardellini, C., Marini, L., & Dietrich, J. H. W. (2002). Geochemical evidences of an ongoing volcanic unrest at nisyros island (greece). *Geophysical Research Letters*, *29*, doi:10.1029/2001GL014355.

Chiodini, G., Caliro, S., Cardellini, C., Granieri, D., Avino, R., Baldini, A., ... Minopoli, C. (2010). Long-term variations of the campi flegrei, italy, volcanic system as revealed by the monitoring of hydrothermal activity. *Journal of Geophysical Research: Solid Earth*, *115*(B3).

Chiodini, G., Frondini, F., Cardellini, C., Granieri, D., Marini, L., & Ventura, G. (2001). Co2 degassing and energy release at solfatara volcano, campi flegrei, italy. *Journal of Geophysical Research: Solid Earth*, *106*(B8), 16213–16221.

Chiodini, G., Paonita, A., Aiuppa, A., Costa, A., Caliro, S., De Martino, P., ... Vandemeulebrouck, J. (2016). Magmas near the critical degassing pressure drive volcanic unrest towards a critical state. *Nature Communications*, *7*(1), 13712. doi: 10.1038/ncomms13712

Chiodini, G., Selva, J., Del Pezzo, E., Marsan, D., De Siena, L., D'auria, L., ... others (2017). Clues on the origin of post-2000 earthquakes at campi flegrei caldera (italy). *Scientific Reports*, *7*(1), 4472.

Chiodini, G., Vandemeulebrouck, J., Caliro, S., D'Auria, L., De Martino, P., Mangiacapra, A., & Petrillo, Z. (2015). Evidence of thermal-driven processes triggering the 2005–2014 unrest at campi flegrei caldera. *Earth and Planetary Science Letters*, *414*, 58-67. doi: doi:10.1016/j.epsl.2015.01.012

Cioni, R., Corazza, E., & Marini, L. (1984). The gas/steam ratio as indicator of heat transfer at the solfatara fumaroles, phlegraean fields (italy). *Bulletin of Volcanology*, *47*, 295–302.

Coco, A., Gottsmann, J., Whitaker, F., Rust, A., Currenti, G., Jasim, A., & Bunney, S. (2016). Numerical models for ground deformation and gravity changes during volcanic unrest: simulating the hydrothermal system dynamics of an active caldera. *Solid Earth*, *7*, 1-21, 10.5194/se-7-1-2016.

Cooper, G. R., & Cowan, D. R. (2008). Edge enhancement of potential-field data using normalized statistics. *Geophysics*, *73*(3), H1–H4.

Cusano, P., Petrosino, S., & Saccorotti, G. (2008). Hydrothermal origin for sustained long-period (lp) activity at campi flegrei volcanic complex, italy. *Journal of Volcanology and Geothermal Research*, *177*(4), 1035–1044.

D'Auria, L., Giudicepietro, F., Aquino, I., Borriello, G., Del Gaudio, C., Lo Bascio, D., ... Ricco, C. (2011). Repeated fluid-transfer episodes as a mechanism for the recent dynamics of campi flegrei caldera (1989-2010). *J. Geophys. Res.*, *116*(B4), B04313. doi: 10.1029/2010jb007837

D'Auria, L., Giudicepietro, F., Martini, M., & Lanari, R. (2012). The 4d imaging of the source of ground deformation at campi flegrei caldera (southern italy). *Journal of Geophysical Research: Solid Earth*, *117*(B8).

Deino, A. L., Orsi, G., de Vita, S., & Piochi, M. (2004). The age of the neapolitan yellow tuff caldera-forming eruption (campi flegrei caldera–italy) assessed by 40ar/39ar dating method. *Journal of Volcanology and Geothermal Research*, *133*(1-4), 157–170.

De Landro, G., Serlenga, V., Russo, G., Amoroso, O., Festa, G., Bruno, P. P., ... Zollo, A. (2017). 3d ultra-high resolution seismic imaging of shallow solfatara crater in campi flegrei (italy): New insights on deep hydrothermal fluid circulation processes. *Scientific Reports*, *7*(1), 3412.

de Lorenzo, S., Gasparini, P., Mongelli, F., & Zollo, A. (2001). Thermal state of the campi flegrei caldera inferred from seismic attenuation tomography. *Journal of geodynamics*, *32*(4-5), 467–486.

De Siena, L., Del Pezzo, E., & Bianco, F. (2010). Seismic attenuation imaging of campi flegrei: Evidence of gas reservoirs, hydrothermal basins, and feeding systems. *J. Geophys. Res.*, *115*(B9), B09312. doi: 10.1029/2009jb006938

Di Giuseppe, M. G., Troiano, A., Fedele, A., Caputo, T., Patella, D., Troise, C., & De Natale, G. (2015). Electrical resistivity tomography imaging of the near-surface structure of the solfatara crater, campi flegrei (naples, italy). *Bulletin* *of Volcanology*, *77*(4), 27. doi: 10.1007/s00445-015-0910-6

Di Luccio, F., Pino, N. A., Piscini, A., & Ventura, G. (2015). Significance of the 1982–2014 campi flegrei seismicity: Preexisting structures, hydrothermal processes, and hazard assessment. *Geophysical Research Letters*, *42*(18), 7498–7506.

Di Vito, M., Isaia, R., Orsi, G., Southon, G., de Vita, S., D'Antonio, M., ... Piochia, M. (1999). Volcanism and deformation since 12,000 years at the campi flegrei caldera (italy). *Journal of Volcanology and Geothermal Research*, *91*, 221-246.

Dobson, P. F., Kneafsey, T. J., Hulen, J., & Simmons, A. (2003). Porosity, permeability, and fluid flow in the yellowstone geothermal system, wyoming. *Journal of Volcanology and Geothermal Research*, *123*(3-4), 313–324.

Eshaghzadeh, A., sadat Kalantari, R., & Hekmat, Z. M. (2015). Optimum density determination for bouguer correction using statistical methods: a case study from north of iran. *International Journal of Advanced Geosciences*, *3*(2), 25–29.

Fedi, M. (2002). Multiscale derivative analysis: A new tool to enhance detection of gravity source boundaries at various scales. *Geophysical Research Letters*, *29*(2), 16–1.

Florio, G., Fedi, M., Cella, F., & Rapolla, A. (1999). The campanian plain and phlegrean fields: structural setting from potential field data. *Journal of Volcanology and Geothermal Research*, *91*(2), 361-379. doi: doi:10.1016/S0377-0273(99)00044-X

Giaccio, B., Hajdas, I., Isaia, R., Deino, A., & Nomade, S. (2017). High-precision 14 c and 40 ar/39 ar dating of the campanian ignimbrite (y-5) reconciles the time-scales of climatic-cultural processes at 40 ka. *Scientific Reports*, *7*, 45940.

Giudicepietro, F., Chiodini, G., Caliro, S., De Cesare, W., Esposito, A. M., Galluzzo, D., ... Vandemeulebrouck, J. (2019). Insight into campi flegrei caldera unrest through seismic tremor measurements at pisciarelli fumarolic field. *Geochemistry, Geophysics, Geosystems*. doi: 10.1029/2019GC008610

Gottsmann, J., & Battaglia, M. (2008). Deciphering causes of unrest at collapse calderas: Recent advances and future challenges of joint gravimetric and ground deformation studies. In J. Gottsmann & J. Marti (Eds.), *Caldera vol-*

canism: Analysis, modelling and response (Vol. 10, p. 417-446). Developments in Volcanology, Elsevier.

Gottsmann, J., Camacho, A., Fernandez, J., & Tiampo, K. F. (2006). Spatio-temporal variations in vertical gravity gradients at the campi flegrei caldera (italy): A case for source multiplicity during unrest? *Geophysical Journal International*, *167*, 1089-1096.

Gresse, M., Vandemeulebrouck, J., Byrdina, S., Chiodini, G., Revil, A., Johnson, T. C., ... Metral, L. (2017). Three-dimensional electrical resistivity tomography of the solfatara crater (italy): Implication for the multiphase flow structure of the shallow hydrothermal system [Journal Article]. *Journal of Geophysical Research: Solid Earth*, *122*(11), 8749-8768. Retrieved from https://doi.org/10.1002/2017JB014389 doi: 10.1002/2017JB014389

Gubbins, D. (2004). *Time series analysis and inverse theory for geophysicists.* Cambridge University Press.

Hammer, S. (1939). Terrain corrections for gravimeter stations. *Geophysics*, *4*, 184-194.

Ingebritsen, S. E., Geiger, S., Hurwitz, S., & Driesner, T. (2010). Numerical simulation of magmatic hydrothermal systems. *Reviews in Geophysics*, *48*(RG1002), doi:10.1029/2009RG000287.

Ingebritsen, S. E., & Sorey, M. (1988). Vapor-dominated zones within hydrothermal systems: Evolution and natural state. *Journal of Geophysical Research: Solid Earth*, *93*(B11), 13635–13655.

Isaia, R., Marianelli, P., & Sbrana, A. (2009). Caldera unrest prior to intense volcanism in campi flegrei (italy) at 4.0 ka bp: Implications for caldera dynamics and future eruptive scenarios. *Geophysical Research Letters*, *36*(21).

Isaia, R., Vitale, S., Di Giuseppe, M. G., Iannuzzi, E., Tramparulo, F. D., & Troiano, A. (2015). Stratigraphy, structure, and volcano-tectonic evolution of solfatara maar-diatreme (campi flegrei, italy). *Geological Society of America Bulletin*, *127*(9-10), 1485-1504. doi: 10.1130/B31183.1

Jasim, A., Whitaker, F. F., & Rust, A. C. (2015). Impact of channelized flow on temperature distribution and fluid flow in restless calderas: Insight from campi flegrei caldera, italy. *Journal of Volcanology and Geothermal Research*, *303*, 157–174.

Knapp, R. B., & Knight, J. E. (1977). Differential thermal expansion of pore fluids: Fracture propagation and microearthquake production in hot pluton environments. *Journal of Geophysical Research*, *82*(17), 2515–2522.

Letort, J., Roux, P., Vandemeulebrouck, J., Coutant, O., Cros, E., Wathelet, M., … Avino, R. (2012). High-resolution shallow seismic tomography of a hydrothermal area: application to the solfatara, pozzuoli. *Geophysical Journal International*, *189*(3), 1725–1733.

Manconi, A., Walter, T. R., Manzo, M., Zeni, G., Tizzani, P., Sansosti, E., & Lanari, R. (2010). On the effects of 3-d mechanical heterogeneities at campi flegrei caldera, southern italy. *J. Geophys. Res.*, *115*(B8), B08405. doi: 10.1029/2009jb007099

Mayer, K., Scheu, B., Montanaro, C., Yilmaz, T. I., Isaia, R., Aßbichler, D., & Dingwell, D. B. (2016). Hydrothermal alteration of surficial rocks at solfatara (campi flegrei): Petrophysical properties and implications for phreatic eruption processes. *Journal of Volcanology and Geothermal Research*, *320*, 128–143.

Montanaro, C., Scheu, B., Mayer, K., Orsi, G., Moretti, R., Isaia, R., & Dingwell, D. B. (2016). Experimental investigations on the explosivity of steam-driven eruptions: A case study of solfatara volcano (campi flegrei). *Journal of Geophysical Research: Solid Earth*, *121*(11), 7996–8014.

Moritz, H. (1992). Geodetic reference system 1980. *Journal of Geodesy*, *66*(2), 187–192.

Nettleton, L. (1976). Gravity and magnetics in oil exploration. *Mac Graw-Hill, New York*.

Nunziata, C., & Rapolla, A. (1981). Interpretation of gravity and magnetic data in the phlegraean fields geothermal area, naples, italy. *Journal of Volcanology and Geothermal Research*, *10*(1-3), 209–225.

Oliveri del Castillo, A., Palumbo, A., & Percolo, E. (1968). Contributo allo studio della solfatara di pozzuoli (campi flegrei) mediante osservazione gravimetriche. *Ann. Oss. Vesuv*, *22*(9), 217–225.

Orsi, G., Civetta, L., Del Gaudio, C., de Vita, S., Di Vito, M., Isaia, R., … Ricco, C. (1999). Short-term ground deformations and seismicity in the resurgent campi flegrei caldera (italy): an example of active block-resurgence in a densely populated area. *Journal of Volcanology and Geothermal Research*, *91*, 415-451.

Parascondola, A. (1947). *I fenomeni bradisismici del sarapeo di pozzuoli.* Naples: Genovese.

Petrosino, S., Cusano, P., & Saccorotti, G. (2006). Shallow shear-wave velocity structure of solfatara volcano (campi flegrei, italy), from inversion of rayleigh-wave dispersion curves. *Bollettino Di Geofisica Teorica Ed Applicata*, *47*(1–2), 89–103.

Petrosino, S., Damiano, N., Cusano, P., Di Vito, M. A., de Vita, S., & Del Pezzo, E. (2012). Subsurface structure of the solfatara volcano (campi flegrei caldera, italy) as deduced from joint seismic-noise array, volcanological and morphostructural analysis. *Geochemistry, Geophysics, Geosystems*, *13*(7).

Piochi, M., Kilburn, C., Di Vito, M., Mormone, A., Tramelli, A., Troise, C., & De Natale, G. (2014). The volcanic and geothermally active campi flegrei caldera: an integrated multidisciplinary image of its buried structure. *International Journal of Earth Sciences*, *103*(2), 401–421.

Ray, R. (1999). A global ocean tide model from topex/poseidon altimetry: Got99. *Technical Report NASA*, *209478*.

Rinaldi, A. P., Todesco, M., Vandemeulebrouck, J., Revil, A., & Bonafede, M. (2011). Electrical conductivity, ground displacement, gravity changes, and gas flow at solfatara crater (campi flegrei caldera, italy): Results from numerical modeling. *Journal of Volcanology and Geothermal Research*, *207*(3-4), 93–105.

Robinson, E. S. (1988). *Basic exploration geophysics.* Somerset, NJ (US); John Wiley and Sons, Inc.

Rosi, M., & Sbrana, A. (1987). *Phlegrean fields* (Vol. 114). Quaderni de la Ricerca Scientifica.

Rowland, J., & Sibson, R. (2004). Structural controls on hydrothermal flow in a segmented rift system, taupo volcanic zone, new zealand. *Geofluids*, *4*(4), 259–283.

Ryan, W. B., Carbotte, S. M., Coplan, J. O., O'Hara, S., Melkonian, A., Arko, R., ... others (2009). Global multi-resolution topography synthesis. *Geochemistry, Geophysics, Geosystems*, *10*(3), 10.1029/2008GC002332.

Saccorotti, G., Petrosino, S., Bianco, F., Castellano, M., Galluzzo, D., La Rocca, M., ... Cusano, P. (2007). Seismicity associated with the 2004–2006 renewed ground uplift at campi flegrei caldera, italy. *Physics of the Earth and Planetary Interiors*, *165*(1-2), 14–24.

Sandwell, D., Garcia, E., Soofi, K., Wessel, P., Chandler, M., & Smith, W. (2013). Toward 1-mgal accuracy in global marine gravity from cryosat-2, envisat, and jason-1. *The Leading Edge*, *32*(8), 892–899.

Sibson, R. H. (1994). Crustal stress, faulting and fluid flow. *Geological Society, London, Special Publications*, *78*(1), 69–84.

Smith, V. C., Isaia, R., & Pearce, N. J. G. (2011). Tephrostratigraphy and glass compositions of post-15 kyr campi flegrei eruptions: implications for eruption history and chronostratigraphic markers [Journal Article]. *Quaternary Science Reviews*, *30*(25), 3638-3660. Retrieved from `http://www.sciencedirect.com/science/article/pii/S0277379111002162` doi: https://doi.org/10.1016/j.quascirev.2011.07.012

Sparks, R. S. J. (2003). Forecasting volcanic eruptions. *Earth and Planetary Science Letters*, *210*, 1-15.

Tamburello, G., Caliro, S., Chiodini, G., De Martino, P., Avino, R., Minopoli, C., ... others (2019). Escalating co2 degassing at the pisciarelli fumarolic system, and implications for the ongoing campi flegrei unrest. *Journal of Volcanology and Geothermal Research*, *384*, 151–157.

Tarquini, S., Vinci, S., Favalli, M., Doumaz, F., Fornaciai, A., & Nannipieri, L. (2012). Release of a 10-m-resolution dem for the italian territory: Comparison with global-coverage dems and anaglyph-mode exploration via the web. *Computers & Geosciences*, *38*(1), 168–170.

Telford, W. M., Geldart, L. P., & Sheriff, R. E. (1991). *Applied geophysics*. Cambridge University Press.

Todesco, M. (2008). Hydrothermal fluid circulation and its effect on caldera unrest. In J. Gottsmann & J. Marti (Eds.), *Caldera volcanism: Analysis, modelling and response* (Vol. Developments in Volcanology, p. 393-416). Elsevier.

Todesco, M., & Berrino, G. (2005). Modeling hydrothermal fluid circulation and gravity signals at the phlegraean fields caldera. *Earth and planetary science letters*, *240*(2), 328–338.

Troiano, A., Di Giuseppe, M. G., Patella, D., Troise, C., & De Natale, G. (2014).

Electromagnetic outline of the solfatara–pisciarelli hydrothermal system, campi flegrei (southern italy). *Journal of Volcanology and Geothermal Research*, *277*, 9–21.

Troiano, A., Isaia, R., Di Giuseppe, M., Tramparulo, F. D. A., & Vitale, S. (2019). Deep electrical resistivity tomography for a 3d picture of the most active sector of campi flegrei caldera. *Scientific Reports*, *9*, 15124.

Troise, C., De Natale, G., Schiavone, R., Somma, R., & Moretti, R. (2019). The campi flegrei caldera unrest: Discriminating magma intrusions from hydrothermal effects and implications for possible evolution. *Earth-Science Reviews*, *188*, 108-122. doi: doi:10.1016/j.earscirev.2018.11.007

Vanorio, T., Virieux, J., Capuano, P., & Russo, G. (2005). Three-dimensional seismic tomography from p wave and s wave microearthquake travel times and rock physics characterization of the campi flegrei caldera. *Journal of Geophysical Research*, *110*(B03201), doi:10.1029/2004JB003102.

Venturi, S., Tassi, F., Bicocchi, G., Cabassi, J., Capecchiacci, F., Capasso, G., … Grassa, F. (2017). Fractionation processes affecting the stable carbon isotope signature of thermal waters from hydrothermal/volcanic systems: The examples of campi flegrei and vulcano island (southern italy). *Journal of Volcanology and Geothermal Research*, *345*, 46–57.

Vilardo, G., Isaia, R., Ventura, G., De Martino, P., & Terranova, C. (2010). Insar permanent scatterer analysis reveals fault re-activation during inflation and deflation episodes at campi flegrei caldera. *Remote Sensing of Environment*, *114*(10), 2373–2383.

Vitale, S., & Isaia, R. (2014). Fractures and faults in volcanic rocks (campi flegrei, southern italy): insight into volcano-tectonic processes. *International Journal of Earth Sciences*, *103*(3), 801–819.

Zollo, A., Capuano, P., & Corciulo, M. (2006). Geophysical exploration of the campi flegrei (southern italy) caldera interiors: Data. *Methods and Results, Doppiavoce, Napoli, Italy*.

Zollo, A., Judenherc, S., Auger, E., d'Auria, L., Virieux, J., Capuano, P., … others (2003). Evidence for the buried rim of campi flegrei caldera from 3-d active seismic imaging. *Geophysical Research Letters*, *30*(19).

Zollo, A., Maercklin, N., Vassallo, M., Dello Iacono, D., Virieux, J., & Gasparini, P.

(2008). Seismic reflections reveal a massive melt layer feeding campi flegrei caldera. *Geophysical Research Letters*, *35*(12).

Table 1. Relevant previous surveys of Solfatara/Pisciarelli (marked S) and the wider Campi Flegrei caldera (marked CFc) pertinent to the hydrothermal system of the caldera's central sector. Question marks (?) indicate undisclosed or unclear survey dates.

Survey Type	Survey Location	Year of Survey	Author
Bouguer Gravity	S	1968	(Oliveri del Castillo et al., 1968)
	S,CFc	2015	This study
Electrical Resistivity	S	>2008	(Di Giuseppe et al., 2015)
	S	2008-2012	(Byrdina et al., 2014)
	S	2013	(Isaia et al., 2015)
	S	2008-16	(Gresse et al., 2017)
	S	2018	(Troiano et al., 2019)
Magnetotellurics	S	2000?	(Bruno et al., 2007)
	S	2012	(Troiano et al., 2014)
Self Potential	S	2011	(Byrdina et al., 2014)
Gas Measurements	S	2011	(Byrdina et al., 2014)
CO_2 flux	S	2012-2019	(Tamburello et al., 2019)
Hydrogeological	S	2000?	(Bruno et al., 2007)
InSAR	CFc	1992-2001, 2003-2007	(Vilardo et al., 2010)
	S,CFc	1995-2007	(D'Auria et al., 2012)

Figure 2. Digital Elevation Models (DEMs) and benchmark locations. a) 10 m DEM of Campi Flegrei caldera with the outline of the major collapse structure (dashed line). Survey benchmarks outside the central sector are shown in blue. Pozzuoli (the centre of ground deformation), Solfatara and Pisciarelli are labelled Po, S and Pi, respectively. b) 1 m DEM of the central sector with the benchmarks in blue including the densely spaced benchmark array in the Solfatara crater.

Table 2. Cont'd.

Survey Type	Survey Location	Year of Survey	Author
P/S-wave velocity	S,CFc	2006?	(Zollo et al., 2006)
	S,CFc	2008	(J. Battaglia et al., 2008)
	S,CFc	2005	(Vanorio et al., 2005)
Seismic reflection	CFc	2008?	(Zollo et al., 2008)
Microseismic	S	2000?	(Bruno et al., 2007)
P wave seismic refraction	S	2000?	(Bruno et al., 2007)
Raleigh wave	S	2000?	(Bruno et al., 2007)
Raleigh waves s-wave velocity	S	2001	(Petrosino et al., 2006)
Seismic tomography	S	2009	(Letort et al., 2012)
Seismic attenuation (passive)	S,CFc	1984	(De Siena et al., 2010)
Seismic noise	S	2007	(Petrosino et al., 2012)
S-wave spectra (passive)	S,CFc	2004-2006	(Saccorotti et al., 2007)
Seismic tremor	S,CFc	2000-2019	(Giudicepietro et al., 2019)
Structural geology	S	2007?	(Petrosino et al., 2012)
	S	2013	(Isaia et al., 2015)
Thermal survey	S	2009-2011	(Byrdina et al., 2014)
Volcanological	S	2007?	(Petrosino et al., 2012)
	S	2012-14	(Isaia et al., 2015)

Figure 1. The Campi Flegrei caldera (14.1°E and 40.8°N) and its main fumarolic areas central sector. a) Google Earth image of the caldera indicating the approximate footprint of ground deformation observed since 1982 (dashed line) and the location of Solfatara and Pisciarelli fumarolic fields (black box). b) Details of the hydrothermal expressions of the Solfatara and Pisciarelli fumarolic fields: Solfatara's fumaroles Bocca Nuova (BN), Bocca Grande (BG) and Le Stufe (LS) and the fence around La Fangaia (LF) are marked by black dashed lines. The main mud-pools and fumaroles of Pisciarelli (Pi) are circled by a dashed yellow line.

Figure 3. Regional and local Bouguer anomaly maps. a) shows the regional Bouguer anomaly, while b) and c) show the local Bouguer anomaly after detrending the data presented in a) for two different components: b) a regional long-wavelength trend to obtain the linearly-detrended residual anomaly (LRA) and c) an additional trend caused by the caldera-fill sediments to obtain the caldera-fill detrended residual anomaly (CRA). The colour bars are scaled to the maximum absolute gravity of the three datasets. Contours are in mGal and benchmarks are shown in white. The data is overlain on the 10 m DEM and Pozzuoli, Solfatara volcano and Astroni volcano are marked by letters P, S and A, respectively.

Figure 4. Local Bouguer anomaly of Solfatara crater. a) LRA, b) CRA. Color bars are not scaled. Contours are in mGal and benchmarks are shown in white. The data is overlain on the 1 m DEM. Black stars mark the locations of La Fangaia (left) and Bocca Grande and Bocca Nuova (right).

Figure 5. First and second total horizontal derivatives of the LRA anomaly and comparison with field structural data. a) displays the first total horizontal derivative (THD1) with interpreted faults shown as dashed black lines and accompanying rose diagrams in b). c) and d) show the same for the second total horizontal derivative (THD2) with interpreted faults marked by dashed yellow lines. e) displays the DEM of the crater floor and mapped faults (Isaia et al., 2015) as dashed blue lines with f) showing the related structural statistics. Data are binned in 10 degree increments in all rose diagrams (b, d and f). f) shows mapped fault orientations (top, dark blue), fracture orientations (bottom, light blue) and the accompanying dip angles presented in (Isaia et al., 2015). Benchmarks are shown by black crosses. Black stars mark the locations of La Fangaia (left) and Bocca Grande and Bocca Nuova (right).

Figure 6. -400 $\mathrm{kg\,m^{-3}}$ density contrast isosurfaces from the optimal inversions for an a priori density contrast of $\pm$ 450 $\mathrm{kg\,m^{-3}}$. a) LRA inversion in plan view. b) LRA inversion with a view facing 59° NE. c) CRA inversion in plan view. d) CRA inversion with view facing 59° NE. e) LRA and CRA inversions in plan view. f) LRA and CRA inversions with view facing 59° NE. The main anomalous bodies are located beneath Pozzuoli, Solfatara/Pisciarelli volcano and Astroni volcano and are labelled P, S and A, respectively.

Figure 7. Surface traces of anomalous bodies for density contrasts of -600, -450 and -300 $\mathrm{kg\,m^{-3}}$ represented by dotted, solid and dashed lines, respectively. a) LRA model. b) CRA model. Location labelings as in Fig. 6.

Figure 8. Diagram of the bulk density contrast parameter space of the proposed hydrothermal reservoirs for scenario 1 (see text for further explanation). A range of phase (solid, liquid, vapour) volume fraction combinations can explain the optimal density contrast of $\sim$ -400 $\pm$25kg m^{-3} and include porous and fractured caldera-fill (host) rocks with an average bulk density of 1900 kg m^{-3} for depths between the surface and 1 km (Piochi et al., 2014)) containing hydrothermal vapour (1.5 kg m^{-3}) and/or liquid (1000 kg m^{-3}) in secondary void space. The optimal anomalous density contrast is highlighted by the gray-colored area and can be explained by a multi-phase mixture of host rock containing a volume fraction of voids between 0.2 and 0.3 that contains a vapour volume fraction of between 0.38 and 1 and a liquid volume fraction of between 0 and 0.62. The red circle marks one of the possible permutation of volume fractions for illustration: solids (0.76) and voids (0.24) with the latter containing vapour (0.8) and liquid (0.2). The colour bar shows the bulk density contrast in kg m^{-3}.

Figure 9. Comparison sketch of previous electrical resistivity (2015) and gravity (1968) anomalies of the Solfatara crater with the LRA data from this study. Dotted lines denote low amplitude anomalies, dashed lines denote moderately low amplitude anomalies and solid lines denote high amplitude anomalies. The crater outline, Pisciarelli, La Fangaia, fumaroles and lava domes are shown. Colour scheme for the LRA gravity anomalies is given in the caption.

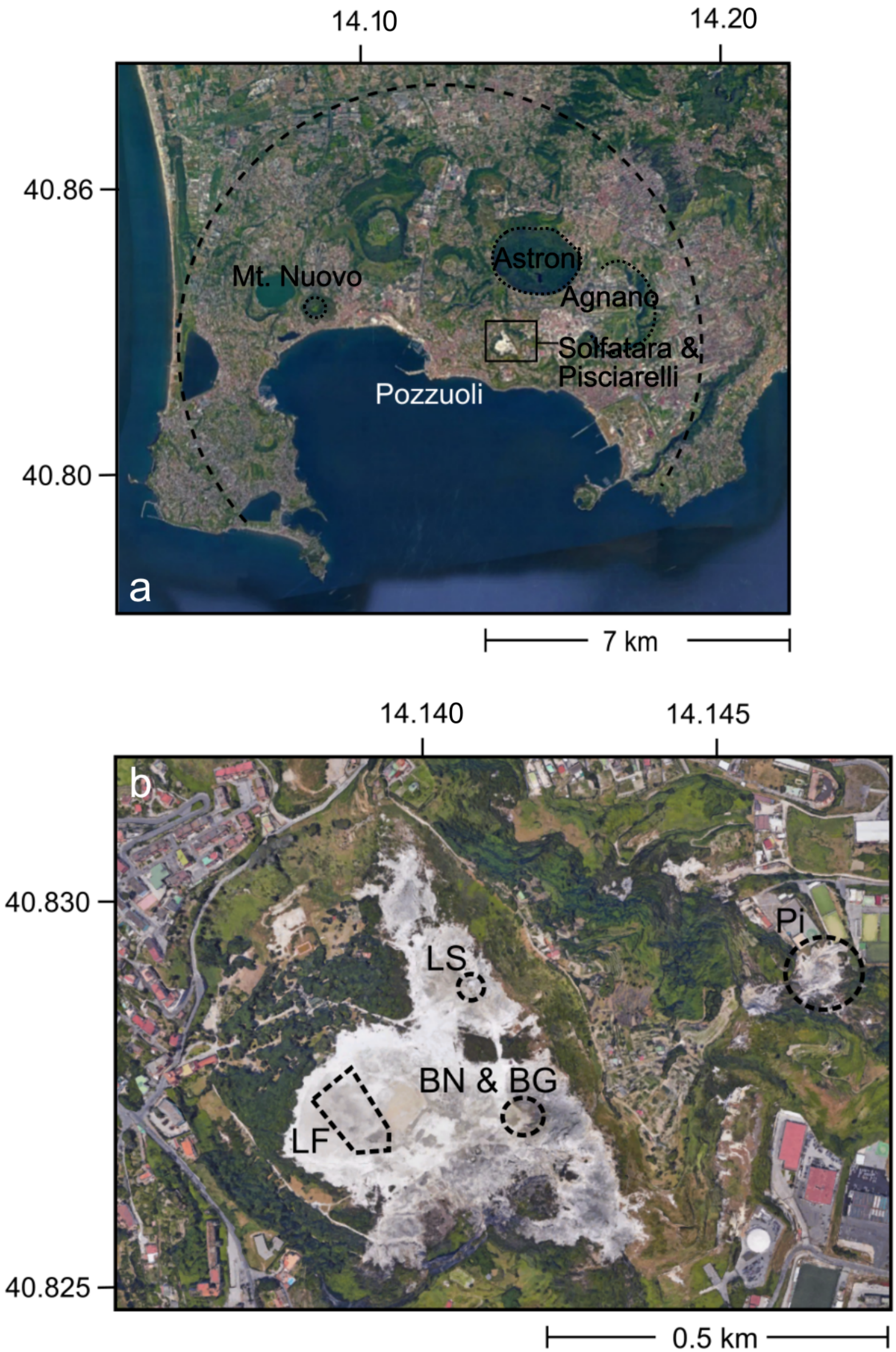
14.10
14.20
40.86
40.80
Mt. Nuovo
Astroni
Agnano
Solfatara &
Pisciarelli
Pozzuoli
a
7 km
14.140
14.145
40.830
40.825
b
LS
Pi
BN & BG
LF
0.5 km

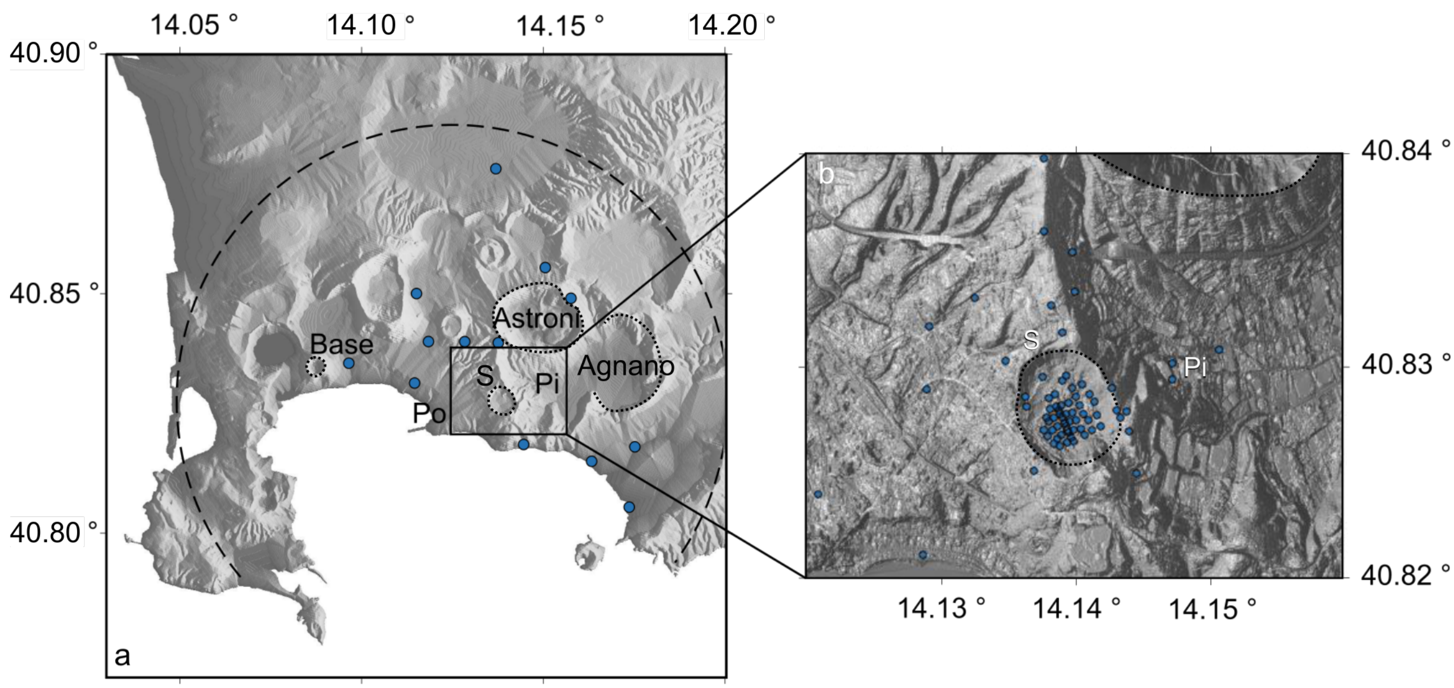
14.05 °
14.10 °
14.15 °
14.20 °
40.90 °
40.85 °
40.80 °
Base
Astroni
Agnano
S
Pi
Po
a
b
40.84 °
40.83 °
40.82 °
14.13 °
14.14 °
14.15 °
S
Pi

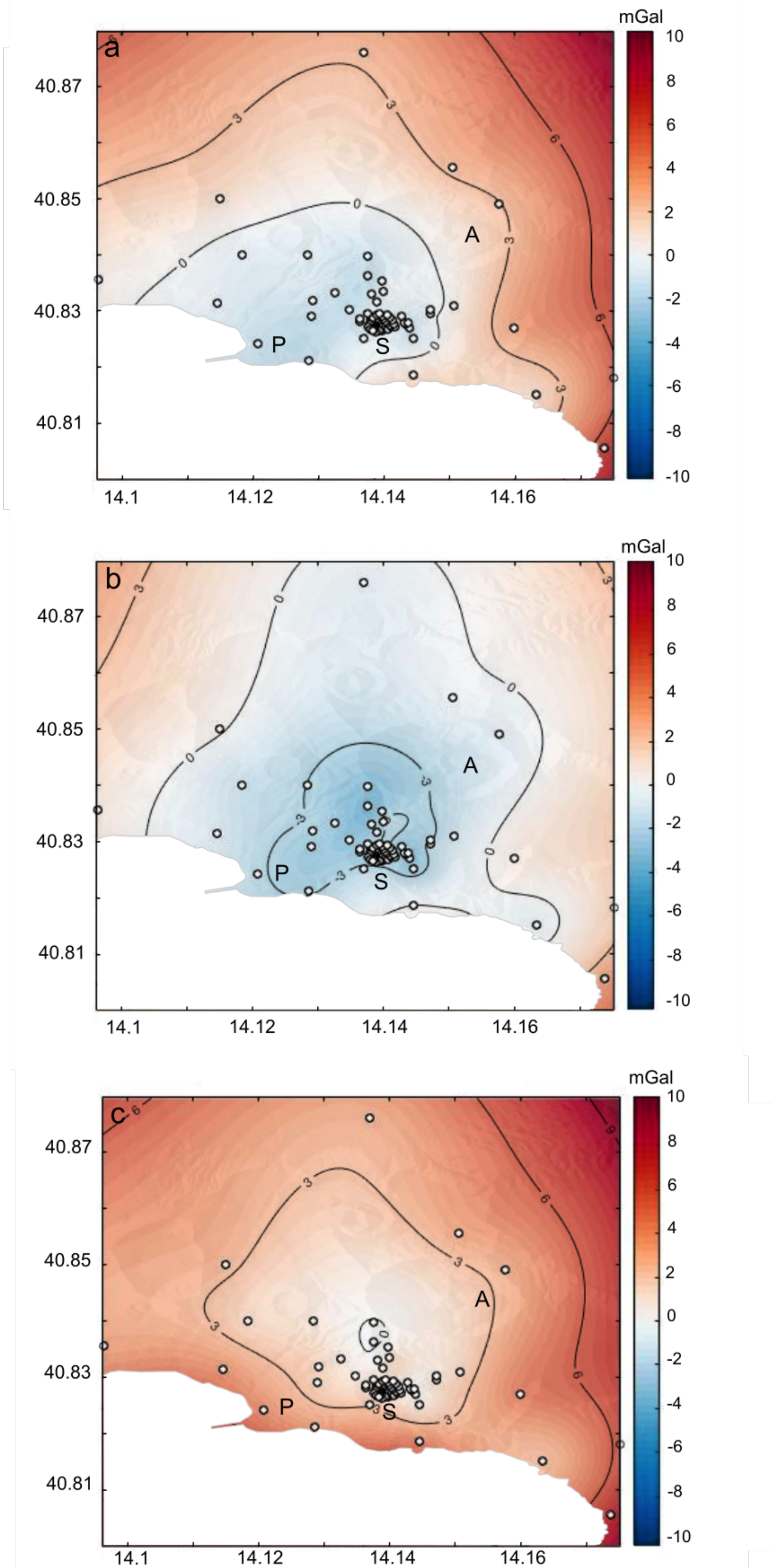
a
b
c
mGal
10
8
6
4
2
0
-2
-4
-6
-8
-10
40.87
40.85
40.83
40.81
14.1
14.12
14.14
14.16
A
P
S
3
0
6
-3

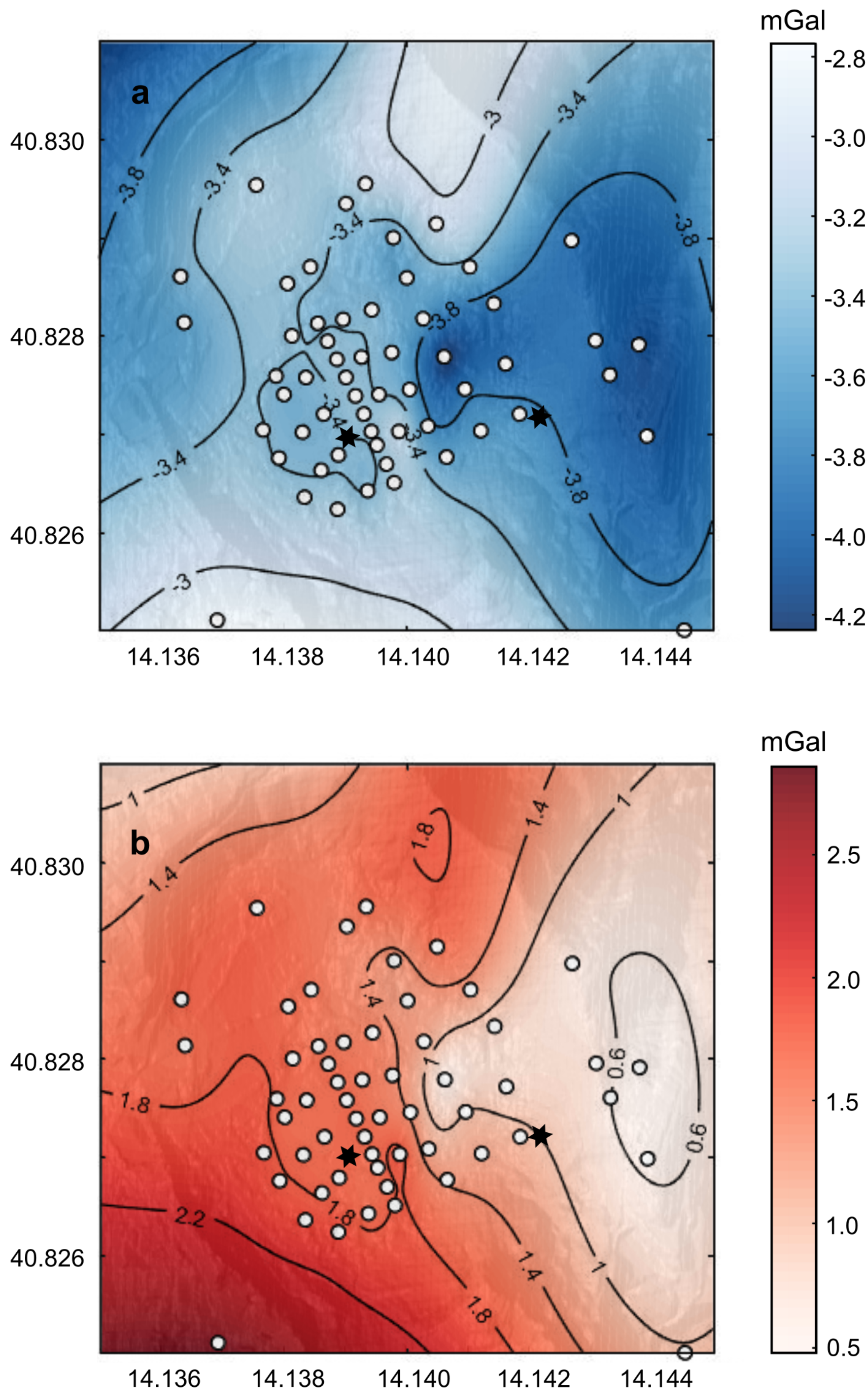
a
b
mGal
-2.8
-3.0
-3.2
-3.4
-3.6
-3.8
-4.0
-4.2
mGal
2.5
2.0
1.5
1.0
0.5
40.830
40.828
40.826
14.136
14.138
14.140
14.142
14.144
-3.8
-3.4
-3
1.8
1.4
1
2.2
0.6

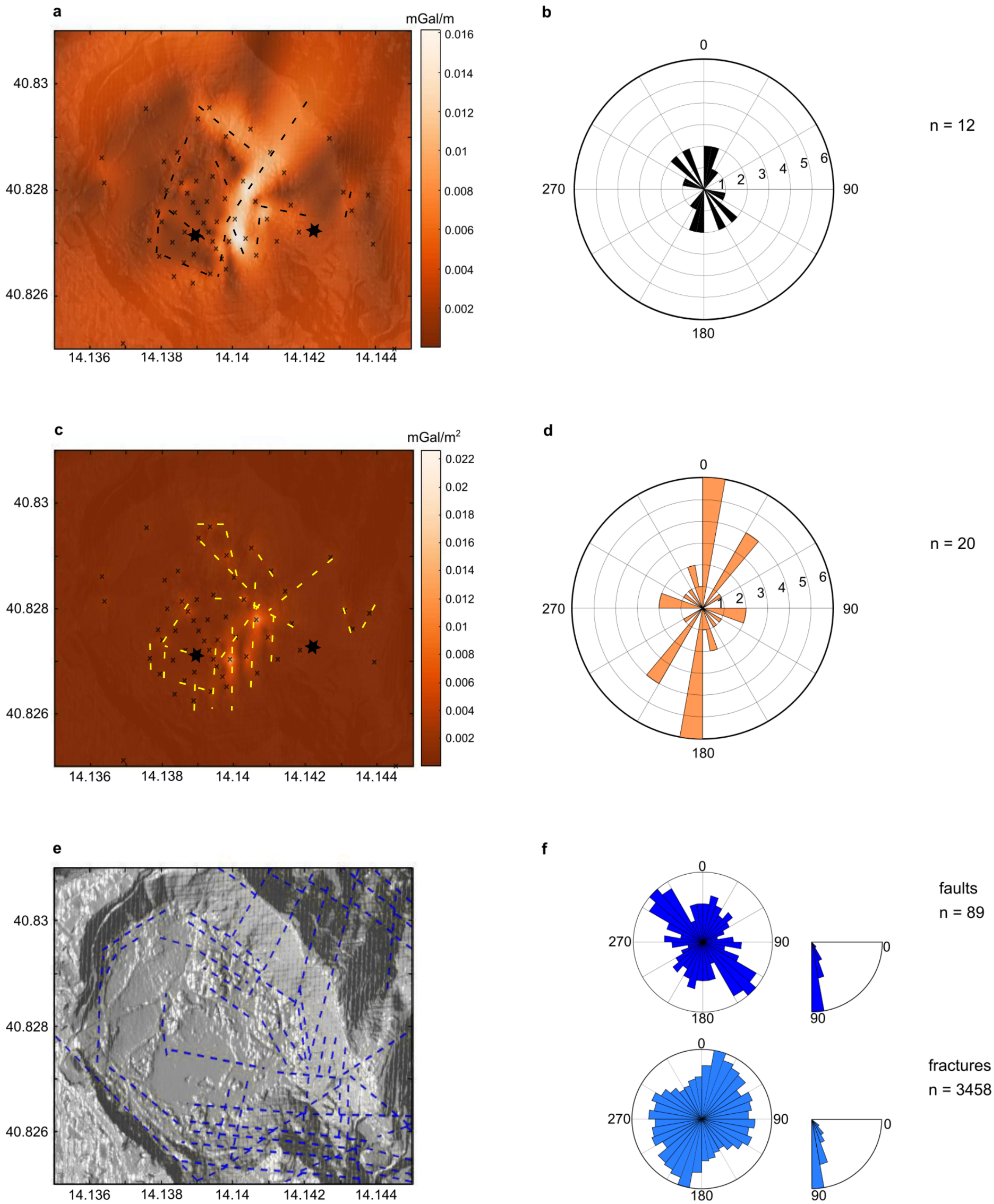
a
mGal/m
0.016
0.014
0.012
0.01
0.008
0.006
0.004
0.002
40.83
40.828
40.826
14.136
14.138
14.14
14.142
14.144
b
0
90
180
270
1
2
3
4
5
6
n = 12
c
mGal/m2
0.022
0.02
0.018
0.016
0.014
0.012
0.01
0.008
0.006
0.004
0.002
40.83
40.828
40.826
14.136
14.138
14.14
14.142
14.144
d
0
90
180
270
1
2
3
4
5
6
n = 20
e
40.83
40.828
40.826
14.136
14.138
14.14
14.142
14.144
f
0
90
180
270
faults
n = 89
fractures
n = 3458

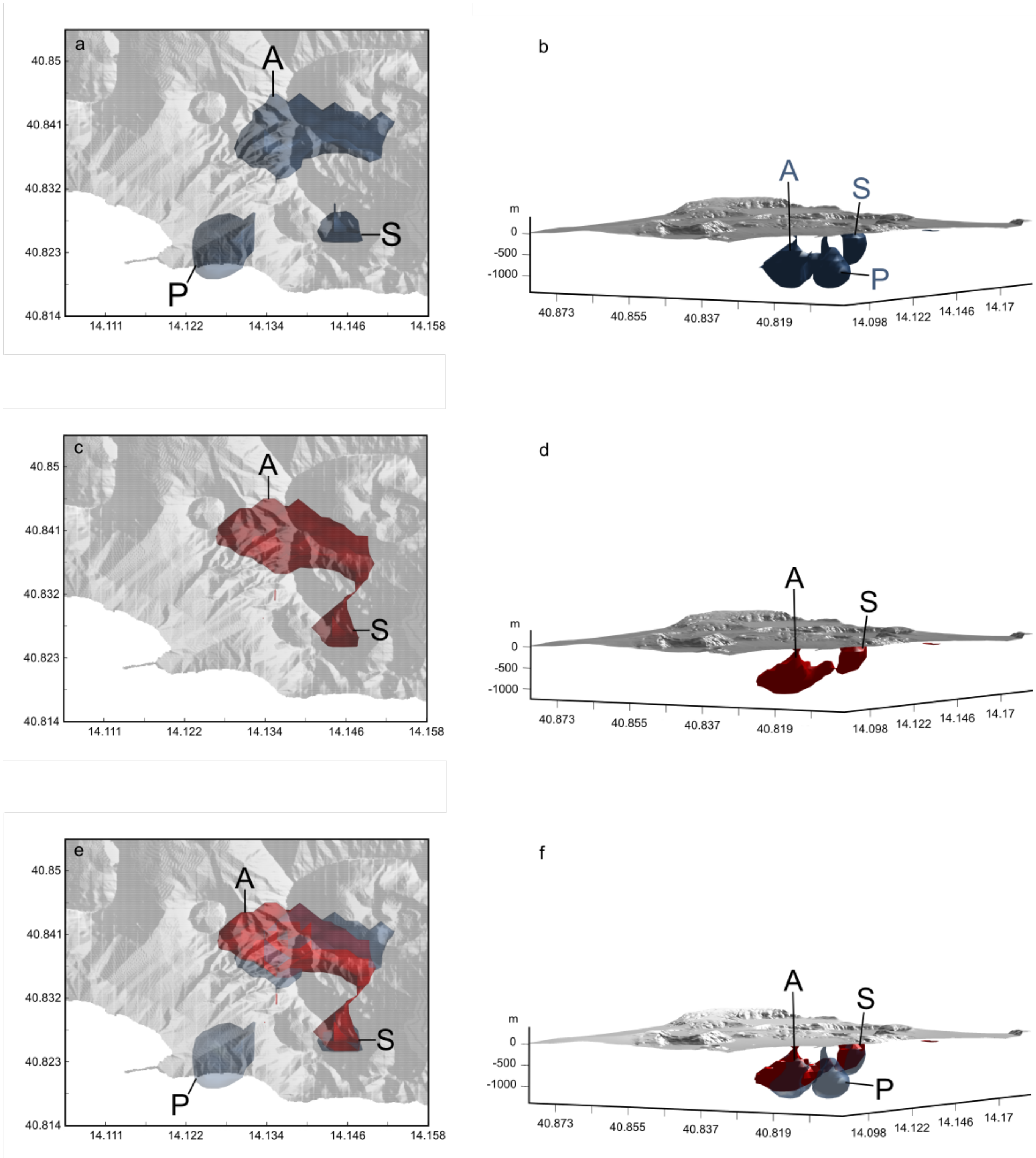

a
A
S
P
40.85
40.841
40.832
40.823
40.814
14.111
14.122
14.134
14.146
14.158
b
A
S
P
m
0
-500
-1000
40.873
40.855
40.837
40.819
14.098
14.122
14.146
14.17
c
A
S
d
A
S
e
A
S
P
f
A
S
P

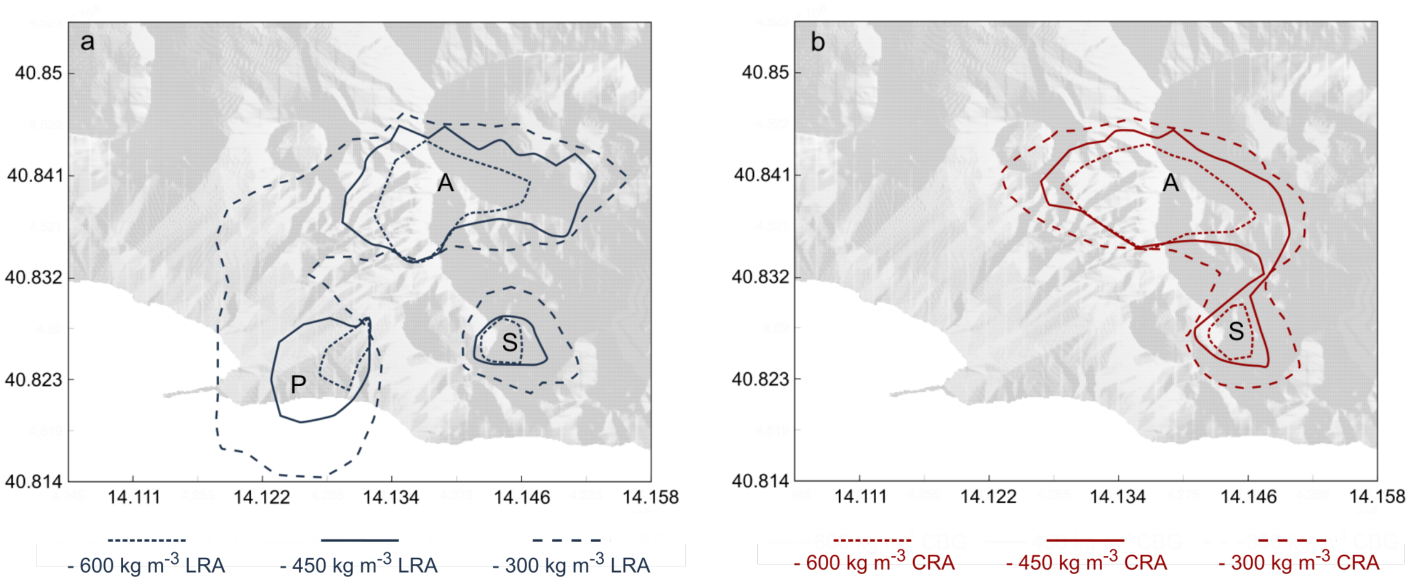
a
40.85
40.841
40.832
40.823
40.814
14.111
14.122
14.134
14.146
14.158
A
P
S
- 600 kg m-3 LRA
- 450 kg m-3 LRA
- 300 kg m-3 LRA
b
A
S
- 600 kg m-3 CRA
- 450 kg m-3 CRA
- 300 kg m-3 CRA

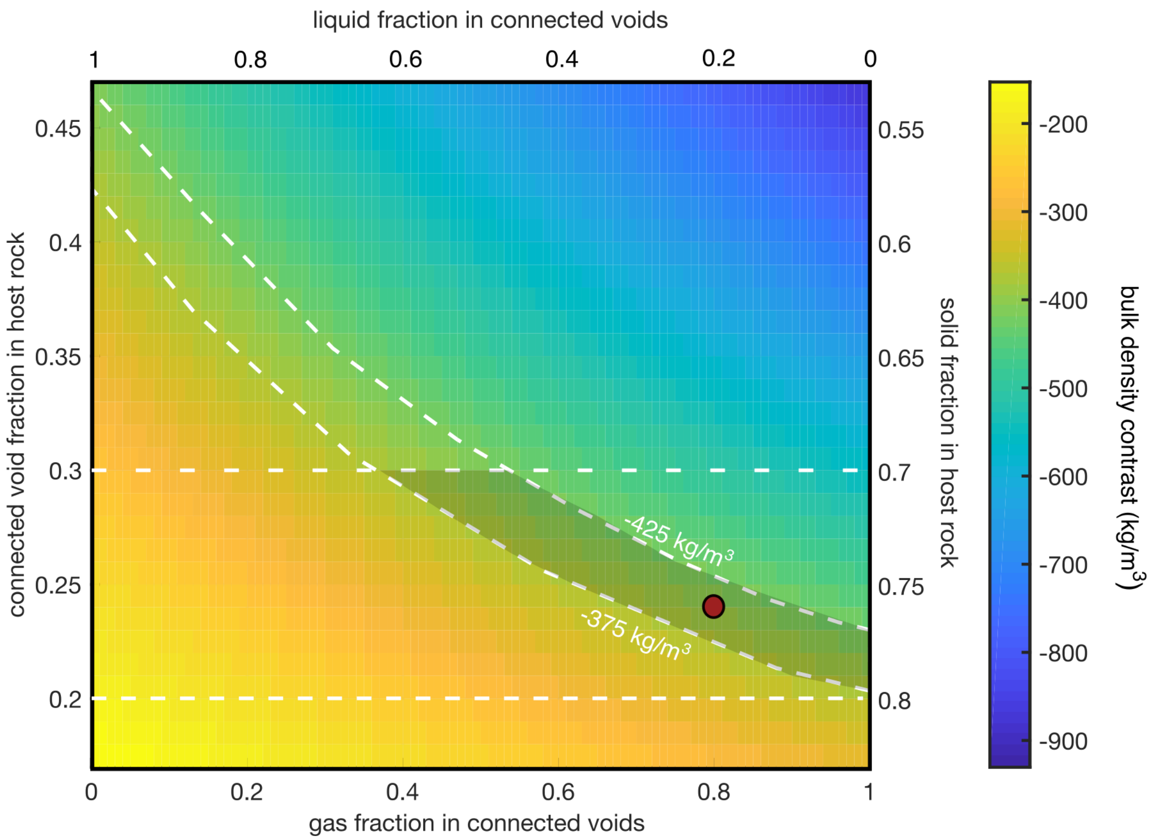

liquid fraction in connected voids
1
0.8
0.6
0.4
0.2
0
connected void fraction in host rock
0.45
0.4
0.35
0.3
0.25
0.2
solid fraction in host rock
0.55
0.6
0.65
0.7
0.75
0.8
-425 kg/m3
-375 kg/m3
gas fraction in connected voids
0
0.2
0.4
0.6
0.8
1
bulk density contrast (kg/m3)
-200
-300
-400
-500
-600
-700
-800
-900

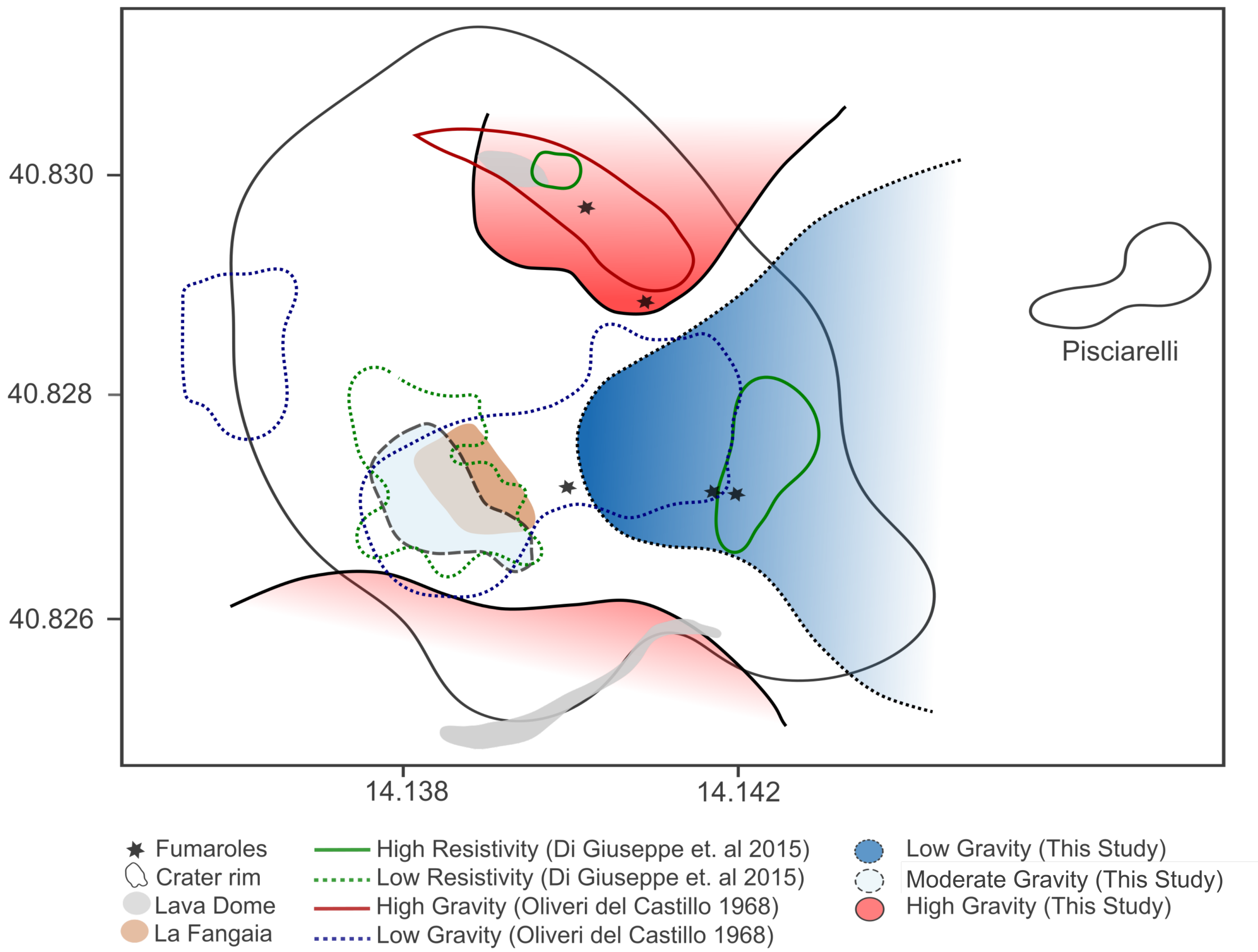

40.830
40.828
40.826
14.138
14.142
Pisciarelli
Fumaroles
Crater rim
Lava Dome
La Fangaia
High Resistivity (Di Giuseppe et. al 2015)
Low Resistivity (Di Giuseppe et. al 2015)
High Gravity (Oliveri del Castillo 1968)
Low Gravity (Oliveri del Castillo 1968)
Low Gravity (This Study)
Moderate Gravity (This Study)
High Gravity (This Study)

Supporting Information for "Gravimetric Constraints on the Hydrothermal System of the Campi Flegrei caldera"

N. Young[1], R. Isaia[2], J. Gottsmann[1*]

[1]School of Earth Sciences, University of Bristol, United Kingdom

[2] Istituto Nazionale di Geofisica e Vulcanologia (INGV), Osservatorio Vesuviano, Italy

Contents of this file

1. Gravity Data Reduction and Correction
2. Information on Caldera Fill Modelling
3. Additional Inversion Models
4. Figures S1 to S7

Introduction This document provides supporting information on the gravity data reduction and inverse modelling as part of the gravity study of the central sector of the Campi Flegrei caldera (Italy).

Corresponding author: J. Gottsmann, School of Earth Sciences, University of Bristol, United Kingdom (gljhg@bristol.ac.uk)

1. Gravity Data Reduction and Correction

1.1. Instrumental Drift

Instrumental drift refers to changes in the instrument with time which affect the reproducibility of measurements. We corrected for drift using standard protocols of conducting single and multiple measurement loops along a series of benchmarks starting and ending at the same reference or control points.

While the drift in the data follows an average linear trend of ∼ -0.675 mGal/day over the course of the survey (Fig. S1), the dataset for each day was corrected using the drift obtained by repeat readings at the base station as well as at control points. For the survey within the Solfatara crater, a control point located just outside the dense survey grid was measured multiple times per day and was tied to the base station twice a day.

1.2. Earth Tides

We used the CG-5 Autograv's inbuilt Earth tide removal algorithm. Ocean loading effects are negligible in the Mediterranean (Ray, 1999) and have not been considered in our survey.

1.3. Normal Gravity

We use the International Gravity Formula (IGF) 1980 (Moritz, 1992) to calculate the normal gravity (g_n) for each gravity benchmark and the gravity reference using:

$$g_n = 978032677.14 \, \frac{1 + 0.0019319 \, sin^2\phi}{(0.0066944 \, sin^2\phi)^2}, \quad (1)$$

where ϕ is the latitude of the station.

Normal gravity at the main gravity base station was calculated at 980244.4306 mGal which all benchmarks were tied to accordingly to account for the effect of latitude on the data.

1.4. Free-Air Correction

The free-air correction (FAC) reduces the gravity data to the same equipotential elevation:

$$FAC(mGal) = -0.3086\, h\,, \tag{2}$$

where h is the height difference in metres from the reference surface. This correction is added to gravity measurements made above the reference surface and subtracted below the reference surface (Telford et al., 1991). -0.3086 mGal/m is the theoretical free-air gradient. Berrino, Corrado, Luongo, and Toro (1984) measured a value of -0.290 mGal/m, and we calculate a value of -0.289 mGal/m from the published Bouguer anomaly data. However, we use the theoretical free-air gradient for the corrections noting that it is a value used more broadly for Bouguer data analysis. Using the theoretical vs the calculated or measured value adds an uncertainty of a few μGal to the Bouguer anomaly given uncertainties in benchmark locations. This error is negligible compared to the uncertainty due to terrain effects (see below). The average error of GPS-derived benchmark elevation of $\pm$ 0.024 m contributes an uncertainty of $\pm$7 μGal to the data based on the theoretical free-air gradient.

The resulting free-air anomaly map is shown in Fig. S2.

1.5. Bouguer Slab and Terrain Correction

The contributions to gravity from rocks located between the elevation of the gravity benchmarks and the elevation of the reference surface is accounted for by the Bouguer slab correction (BS) and the terrain correction (TC). The Bouguer slab correction (Bullard A) approximates this material as a slab of infinite horizontal extent, finite thickness and constant density (Robinson, 1988)

$$BS(mGal) = -0.0419\,\rho\,h, \tag{3}$$

where ρ is the density of the slab (described below) and h is the height difference (m) from the reference datum.

The uncertainty of benchmark elevations and the tested density increments ($100\,\mathrm{kg\,m^{-3}}$) generates an uncertainty of 4 μGal in the BS correction.

The approximation of the Bouguer slab only holds if the nearby topography is extremely subdued (Robinson, 1988). This is not the case at Campi Flegrei and one must consider an additional terrain correction, which we perform in MATLAB using high resolution onshore Digital Elevation Models (DEMs). Within and nearby the steep sided Solfatara crater, we used a 1 m DEM. We took care to place benchmarks in locations free from significant nearby (within the first Hammer zone) topographic changes to mitigate the effects of near-field topography. A 10 m DEM (Tarquini et al., 2012) was appropriate for the more distal region surrounding Solfatara. The RMS error between the GPS benchmark heights and heights at the same locations in the DEMs was ∼2 m and ∼0.4 m for the 10 m and the 1 m DEMs, respectively. We accounted for these offsets in the processing. We also incorporated bathymetric data (Ryan et al., 2009) to calculate terrain effects induced by offshore topography. As the density of sea water ($1024\,\mathrm{kg\,m^{-3}}$) is much lower than that of rock this must be accounted for separately in the terrain correction.

We constructed separate DEMs for the onshore and offshore portions of the terrain correction. To test the uncertainty of the terrain correction by offsets between DEM heights and GPS derived heights we generated two normally distributed random topographies, ranging from 0 m in height to the RMS error between the GPS benchmark heights and 10 m and 1 m DEM heights (2 m and 0.4 m, respectively). We calculated the terrain correction for two benchmarks located 1 km apart (for the 10 m DEM) and 50 m apart (for the 1 m DEM) to establish the difference between the two terrain corrections. This was repeated 100 times and the 1 σ error of each distribution was found to be 130 μGal and 13 μGal for the 10 m and 1 m DEM, respectively.

To calculate the cumulative terrain effect we followed the approach of Hammer (1939), but calculated the terrain correction at each DEM data point rather than for each Hammer chart compartment. The distance from each benchmark to every DEM data point is calculated and used to weigh the influence of the height difference between each DEM data point and the benchmark;

$$TC_1 = \left(\frac{1}{r} - \frac{1}{r^2 + \Delta z^2}\right) \Delta x^2, \qquad (4)$$

where r is the radial distance from the benchmark to each DEM data point in metres, Δz is the height difference between the benchmark and the DEM data point and Δx is the DEM spacing. The total terrain correction for each benchmark is then calculated;

$$TC_2 = \rho G \sum TC_1, \quad (5)$$

where G is the universal gravitational constant. The terrain correction was calculated for the onshore portion of the survey using the onshore DEM and an appropriate density (described below). The offshore portion required a density equal to that of the onshore density minus the density of seawater (1024 kg m^{-3})

The density for both the Bouguer correction and the terrain correction should be close to the average sub-surface density (Robinson, 1988). If density data is not available it is possible to estimate it using the Bouguer anomaly and elevation data. Traditionally this is done using the Nettleton method (Nettleton, 1976). This method involves plotting profiles of Bouguer gravity (for a range of different terrain densities) against topography and calculating the correlations between the Bouguer anomalies for a range of different terrain densities and topography. The terrain density giving the least correlation between Bouguer anomaly and topography is selected as the best estimate of terrain density. (Fig. S3) However, profiles over structurally controlled features may not be appropriate as density might change with elevation (Nettleton, 1976). While the profiles displayed in Fig. S3 show some correlation with topography, the least correlated profile is between 1800 and 1900 kg m^{-3}. The interpolation of the Bouguer gravity data has a smoothing effect particularly in areas of sparse data and makes correlating the elevation and Bouguer gravity profiles qualitative rather than quantitative.

To explore a quantitative approach we correlate the Bouguer anomaly for different terrain densities with elevation at each benchmark (Eshaghzadeh et al., 2015). This correlation is plotted against the tested densities and a least-squares straight line is fitted to the resultant data. Once this line is subtracted from the data, the 'correlation difference' is plotted against the density and returns an unique optimal terrain density. The resultant value of 1900 kg m^{-3} (Fig. S4) is in agreement with the value derived by the Nettleton method and compares with densities of material recovered from boreholes at Campi Flegrei in the range from ∼1600 kg m^{-3} (tuff) to ∼2800 kg m^{-3} (thermometamorphic rocks) (Barberi et al., 1991; Piochi et al., 2014). The average density of the first 500 m of all borehole data is approximately 1800 kg m^{-3} and the average density of all the borehole data is 2300 kg m^{-3} (Barberi et al., 1991). We hence regard the value of 1900 kg m^{-3} for both the terrain and Bouguer slab densities as a mathematically robust and geologically plausible estimate.

2. Caldera Fill Modelling

The effect of the caldera fill on the regional Bouguer anomaly is shown in Fig. S5.

3. Inversion Models for ±600 and ±300 kg m^{-3} A Priori Density Contrasts

Results are shown in Figs. S6 and S7.

References

Barberi, F., Cassano, E., La Torre, P., & Sbrana, A. (1991). Structural evolution of campi flegrei caldera in light of volcanological and geophysical data. *Journal of Volcanology and Geothermal Research*, *48*(1-2), 33–49.

Berrino, G., Corrado, G., Luongo, G., & Toro, B. (1984). Ground deformation and gravity changes accompanying the 1982 pozzuoli uplift. *Bulletin of Volcanology*, *47*(2), 188-200.

Capuano, P., Russo, G., Civetta, L., Orsi, G., D'Antonio, M., & Moretti, R. (2013). The active portion of the campi flegrei caldera structure imaged by 3-d inversion of gravity data. *Geochemistry, Geophysics, Geosystems*, *14*(10), 4681–4697.

Eshaghzadeh, A., sadat Kalantari, R., & Hekmat, Z. M. (2015). Optimum density determination for bouguer correction using statistical methods: a case study from north of iran. *International Journal of Advanced Geosciences*, *3*(2), 25–29.

Hammer, S. (1939). Terrain corrections for gravimeter stations. *Geophysics*, *4*, 184-194.

Moritz, H. (1992). Geodetic reference system 1980. *Journal of Geodesy*, *66*(2), 187–192.

Nettleton, L. (1976). Gravity and magnetics in oil exploration. *Mac Graw-Hill, New York*.

Piochi, M., Kilburn, C., Di Vito, M., Mormone, A., Tramelli, A., Troise, C., & De Natale, G. (2014). The volcanic and geothermally active campi flegrei caldera: an integrated multidisciplinary image of its buried structure. *International Journal of Earth Sciences*, *103*(2), 401–421.

Ray, R. (1999). A global ocean tide model from topex/poseidon altimetry: Got99. *Technical Report NASA*, *209478*.

Robinson, E. S. (1988). *Basic exploration geophysics*. Somerset, NJ (US); John Wiley and Sons, Inc.

Ryan, W. B., Carbotte, S. M., Coplan, J. O., O'Hara, S., Melkonian, A., Arko, R., ... others (2009). Global multi-resolution topography synthesis. *Geochemistry,* *Geophysics, Geosystems*, *10*(3), 10.1029/2008GC002332.

Tarquini, S., Vinci, S., Favalli, M., Doumaz, F., Fornaciai, A., & Nannipieri, L. (2012). Release of a 10-m-resolution dem for the italian territory: Comparison with global-coverage dems and anaglyph-mode exploration via the web. *Computers & Geosciences*, *38*(1), 168–170.

Telford, W. M., Geldart, L. P., & Sheriff, R. E. (1991). *Applied geophysics.* Cambridge University Press.

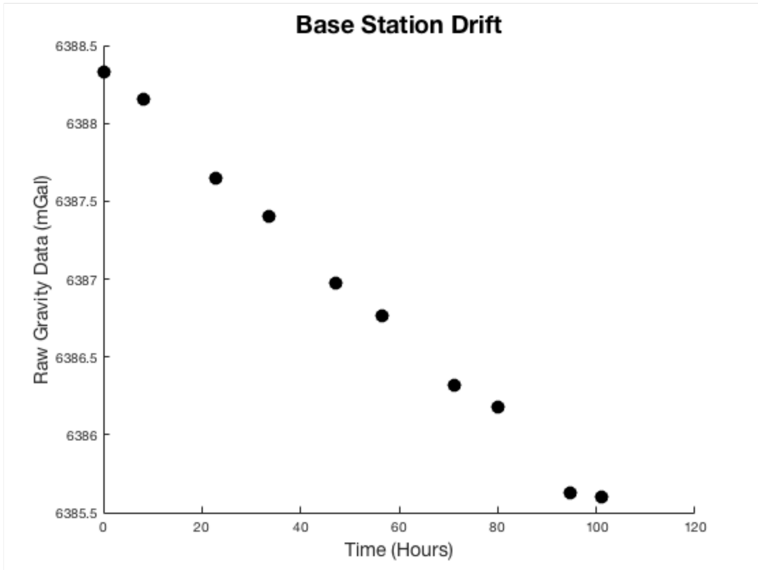

Figure S1. Instrument drift of ∼ -0.675 mGal/day established by gravity readings at the base station over the course of the survey.

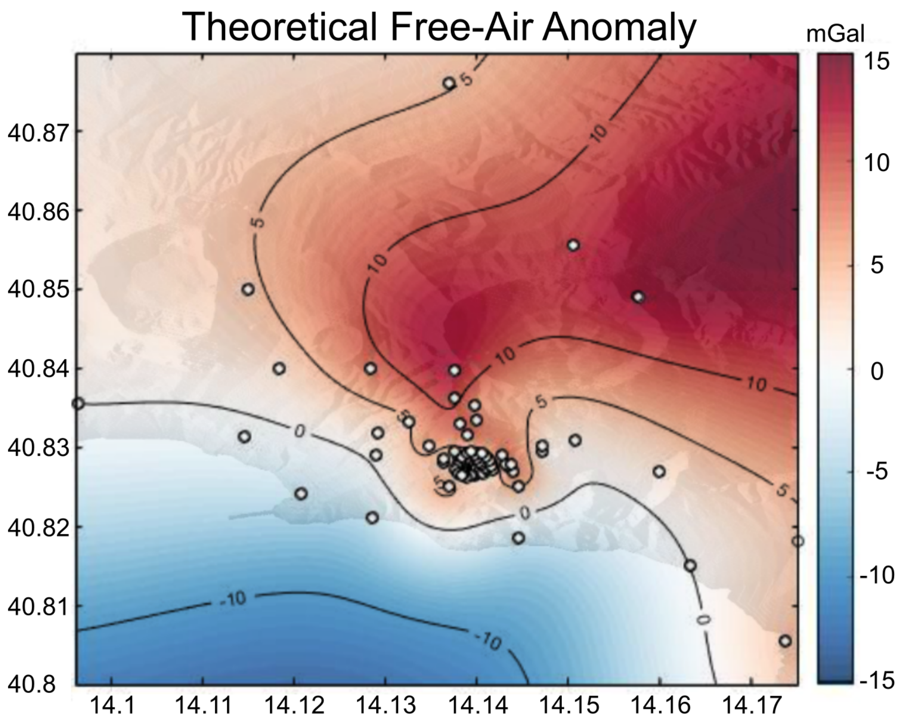

Figure S2. Free-air anomaly map superimposed on the 10 m DEM with benchmarks in white and contours in mGal.

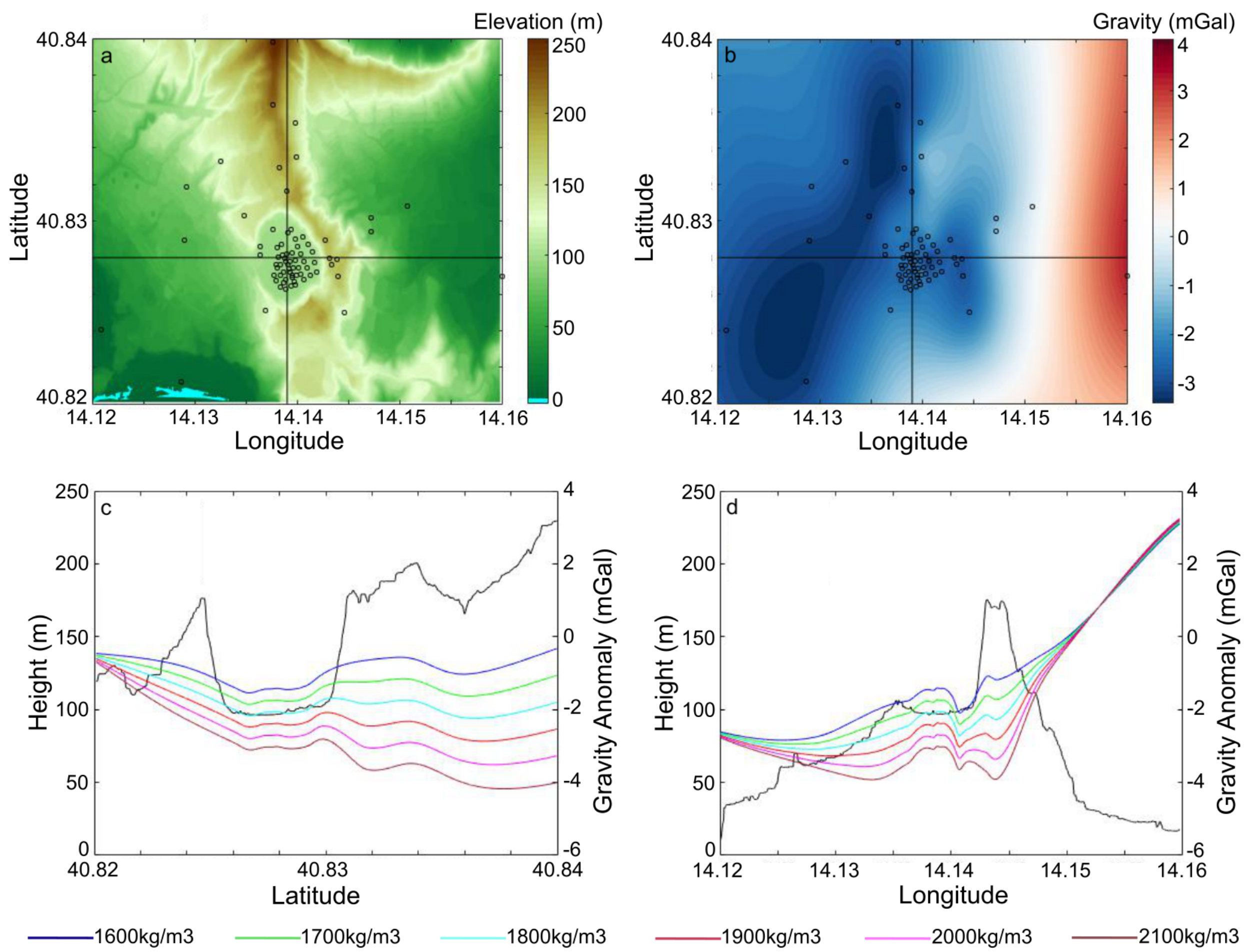

Figure S3. Derivation of the terrain density using Nettleton's method. a) The 1m DEM with EW and NS profiles at 40.828°N and 14.139°E, respectively shown as black lines. b) Bouguer anomaly map for a 1900 kg m^{-3} Bouguer slab and terrain density with NS and EW profiles shown as black lines. c) Comparison of Bouguer anomaly data (for slab and terrain densities as per the legend) with topography (black line) along the N-S profile. d) same as c) for the EW profile.

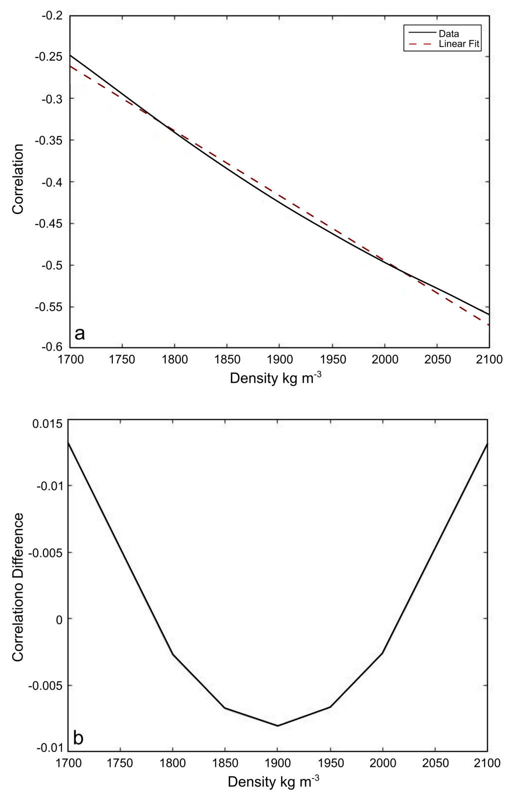

Figure S4. a) Correlation between topography and terrain density with the best linear fit (dashed red line). b) The residuals between the correlation curve and its linear trend plotted against density yields an unique minimum value of the terrain density which minimises the topographic effects on the Bouguer anomaly (Eshaghzadeh et al., 2015).

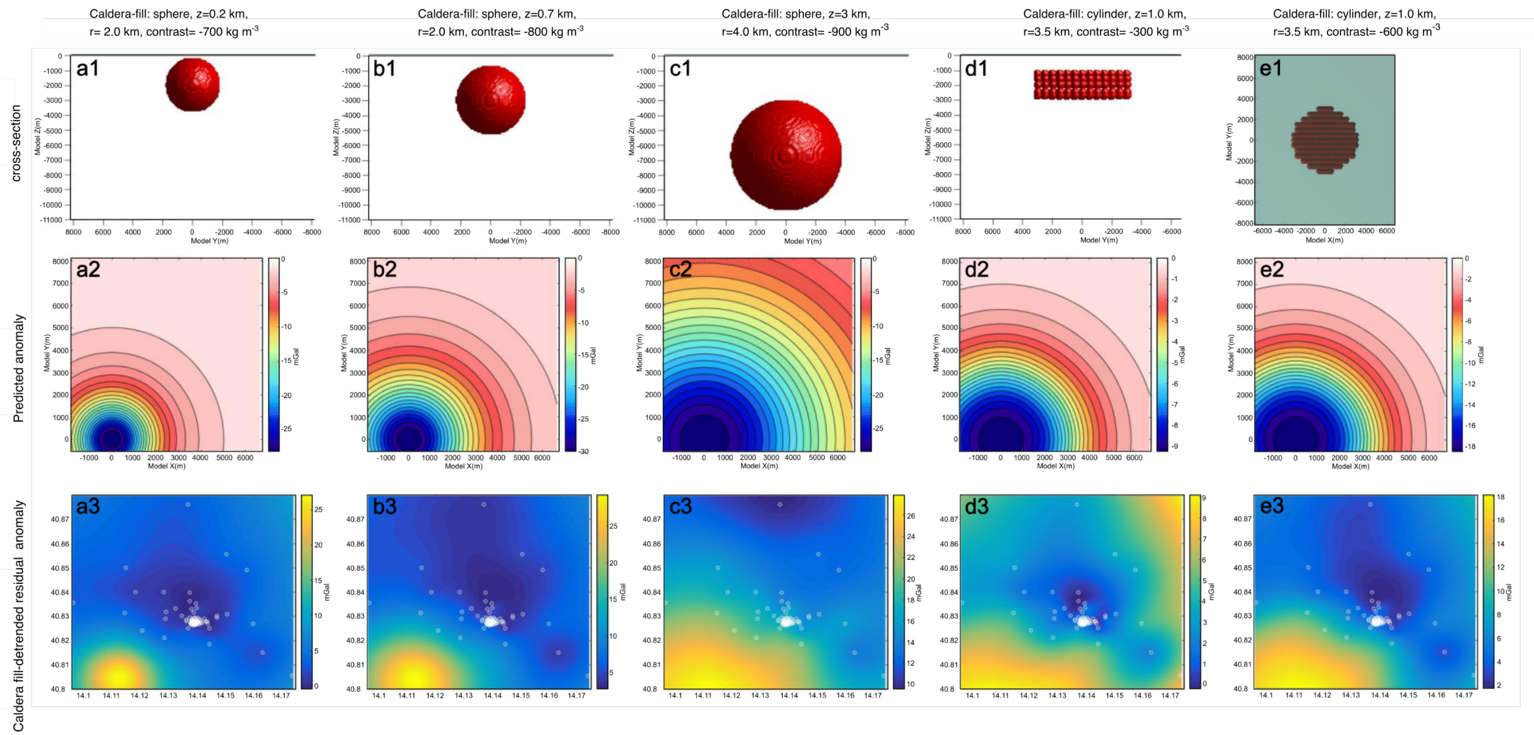

Figure S5. The effect of the caldera fill on the regional Bouguer anomaly for spherical (panel letters a-c) and cylindrical (panel letters c and d) representations of the fill. Panels numbers (1) show model cross sections for given shape, depth to top of body (z) and radius (r) and negative density contrast, except for e1 which illustrates the model shown in d1 in plan view. Panels numbers (2) give the predicted gravity anomaly at the surface. Panel numbers (3) show the resultant local Bouguer gravity anomaly once the caldera fill anomaly has been subtracted from the regional Bouguer data set to obtain the caldera-fill detrended residual anomaly (CRA) (see main text for details). The single sphere models (panels a-c) were rejected for lack of fitting with results from gravity modeling presented by (Capuano et al., 2013), while the cylinder models (panels d-e) provided a much better match with d3 providing the best. The resultant CRA shown in d3 is identical to the CRA presented in Fig. 3c of the main paper and is used for the inversions.

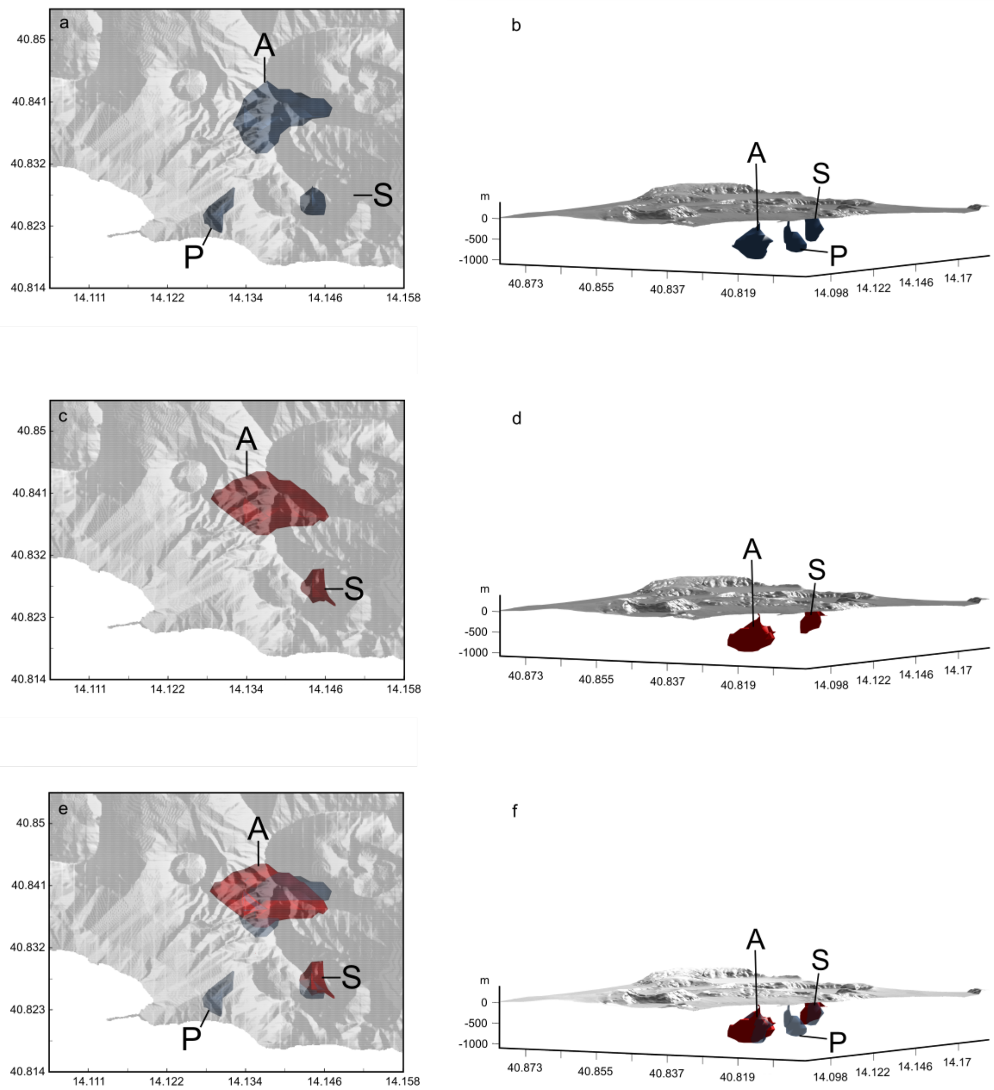

Figure S6. -550 kg m^{-3} density contrast isosurfaces from inversions with an a priori density contrast of ± 600 kg m^{-3}. a) LRA inversion in plan view. b) LRA inversion with a view facing 59° NE. c) CRA inversion in plan view. d) CRA inversion with view facing 59° NE. e) LRA and CRA inversions in plan view. f) LRA and CRA inversions with view facing 59° NE. The main anomalous bodies are located beneath Pozzuoli, Solfatara/Pisciarelli volcano and Astroni volcano and are labelled P, S and A, respectively.

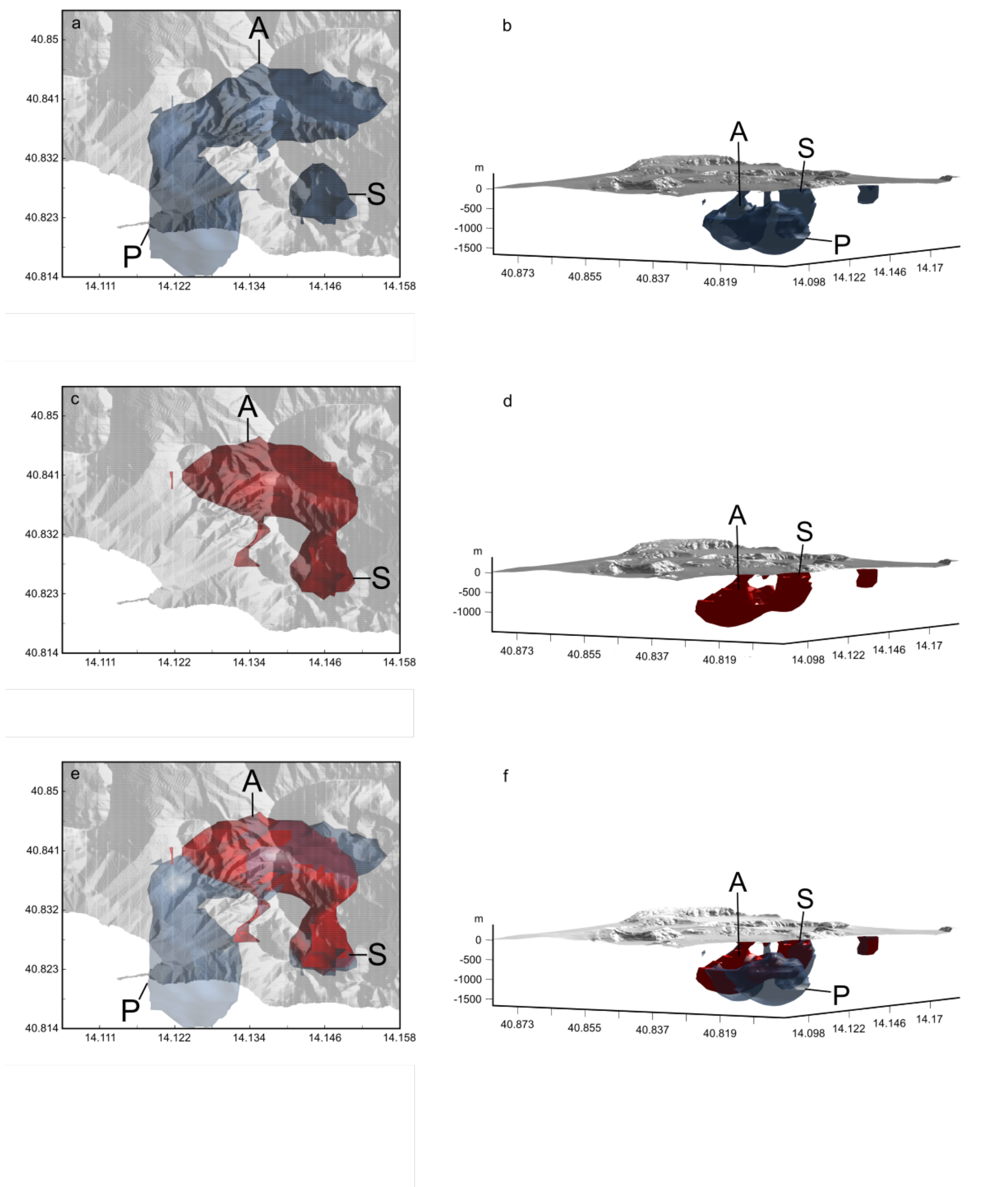

Figure S7. Same as Figure S6 but showing the -250 $\mathrm{kg\,m^{-3}}$ density contrast isosurfaces from inversions with an a priori density contrast of $\pm$ 300 $\mathrm{kg\,m^{-3}}$.